STRESS TENSOR SYMMETRY PRESERVING MODEL APPLIED TO THE 2-D VISCOELASTIC FLOW OF A BIOFILM

by

Daniel Bert Kanewske

A dissertation submitted in partial fulfillment
of the requirements for the degree

of

Doctor of Philosophy

in

Mathematics

MONTANA STATE UNIVERSITY
Bozeman, Montana

November, 2016

©COPYRIGHT

by

Daniel Bert Kanewske

2016

All Rights Reserved

DEDICATION

I dedicate this to my son Oliver. No matter how difficult your life becomes, never give up!

ACKNOWLEDGEMENTS

I would like acknowledge Dr. Tianyu Zhang, without his assistance I would never have completed my work. Dr. Zhang has taught me much of the mathematics that I have used in this work. He is also a kind, gentle and brilliant man whom I aspire to be more like. I would also like to thank the committee for helping me finish my dissertation and the math department, who guided my mathematical development and proved financial support which has made this possible. I would also like to thank Gary Sackett for his financial assistance. Mark, for always being there.

TABLE OF CONTENTS

1. INTRODUCTION 1

Thesis Organization: 15

2. MODEL OF BIOFILM AS VISCOELASTIC FLUID 16

Model: 17
Viscoelastic Fluid: 17
Navier-Stokes Equation: 19
Incompressibility: 21
Stress: 21
Stress Development: 22
Advection Equation: 33
Eulerian Lagrangian Method: 33
Finite Element Model: 35
Initial Conditions: 40
Boundary Conditions: 41

3. NUMERICAL METHODS 45

Numeric Model: 45
Algorithm: 45
Softening Diffusion: 47
Departure Feet: 47
Finite Element: 50
Navier-Stokes: 51
Stress: 56
Advection: 59

4. RESULTS 62

Results: 63
Hidden CFL-type Problem: 63
Velocity: 65
Horizontal Velocity: 65
Vertical Velocity: 66
Pressure: 67
Stress: 70
XX-Stress Component: 71

TABLE OF CONTENTS - CONTINUED

XY-Stress Component: 71
YY-Stress Component: 72
Incompressibility: 73
Non-linesar Inertia Term: $\mathbf{u}\nabla\mathbf{u}$ 74
Vorticity: 75
Parameter Variations: 76
Biofilm Viscosity: 76
GLS: 77
Johnson-Segalman: 77

5. CONCLUSION 80

REFERENCES CITED 82

LIST OF TABLES

Table Page

2.1 Model Nomenclature 20

2.2 Characteristic Deformation 23

2.3 13 Point 2-D Gaussian Quadrature 39

2.4 4 Point 1-D Gaussian Quadrature 40

4.1 List of parameters used in most simulations 62

LIST OF FIGURES

Figure		Page
1.1	Viscoelastic Fluid responce to shear	8
1.2	Model domain schematic	11
2.1	Flow line	22
2.2	Flow line with departure feet	34
2.3	A 4X4 triangle partitioning	36
2.4	Reference Triangle	36
2.5	Initial biofilm volume fraction diffusion effects	41
2.6	Domain and boundaries	42
4.1	Initial biofilm volume fraction after diffusion	63
4.2	CFL type instability	64
4.3	Horizontal velocity after 100 time steps	65
4.4	Four different biofilm surfaces	66
4.5	Comparing several horizontal velocity surfaces	67
4.6	Vertical velocity after 100 time steps	68
4.7	Equilibrium velocities	69
4.8	Pressure after 100 time steps	70
4.9	Flat initial biofilm surface	70
4.10	Flat biofilm pressure surface	71
4.11	Flat biofilm mesh refinement surfaces	72
4.12	Horizontal stress surface	73
4.13	Diagonal stress surface	73
4.14	Vertical stress surface	74
4.15	Incompressibility condition	74
4.16	Non-linear inertia term	75

LIST OF FIGURES - CONTINUED

Figure Page

4.17 Vorticity 76

4.18 Viscosity comparison 77

4.19 Galerkin least squares parameter comparison 78

4.20 Slippage parameter comparison 79

ABSTRACT

The symmetry of the numeric representation of the stress tensor has been shown to be important for maintaining stability, in the sense of Hadamard, of the numeric method. Also, the viscoelastic behavior of biofilms is well documented. A 2D model for the viscoelastic flow of a biofilm using a modified Navier-Stokes equation (NSE) with a novel elastic stress term are presented. The elastic stress is modeled using a numeric stress tensor symmetry preserving scheme that is based on the numeric solution to the Lie derivative and its equivalent counterpart in the form of a symmetric matrix Riccati differential equation (SMRDE). In addition, a coupled advection equation (AE) is applied to the biofilm volume fraction. Solutions to the NSE and AE are found by applying the finite element method (FEM) to the Eulerian-Lagrangian method (ELM). The ELM is solved by first determining the "characteristic foot" for each Gaussian quadrature point and node point in the mesh. The advection equation is solved using a modified Galerkin Least Squares (GLS) method. Computations are made using the Trilinos iterative sparse matrix solver library called AztexOO which has built in matrix preconditioners and support for parallel processing. The resulting model is used to predict the deformation of a biofilm in a 2D channel. In addition, the accompanying distribution of the pressure and stresses over the evolving velocity field is presented.

1

INTRODUCTION

A biofilm is a colony of bacteria suspended in a collection of polymers, produced by the bacteria, called extracellular polymeric substance, a.k.a., EPS. There are two definitions for a biofilm used by the IWA task group [57], on biofilm modeling. The first is, microorganisms attached to a surface. The benefit of this simply definition is that it captures the difficulty in defining such a diverse collection of biologically generated structures. The second definition is more technical and is, "a layer of prokaryotic and eukaryotic cells anchored to a substratum surface and embedded in an organic matrix of biological origin.". One may note that the second definition does not give any insight that is a significant improvement over the first. Westall [59] found biofilm micro-colonies on the order of μm in the South African Kromberg formation. The Kromberg is roughly 3.3 - 3.4 billion years old. This long duration of existence has allowed biofilms to adapt and evolve with the evolution of more complex animals. So, it is no wonder that biofilms thrive almost everywhere that there is enough moisture and nutrients to support growth. While biofilms are composed and created by simple organisms they do exhibit interesting and dynamic structures and behaviors. A better understanding of the mechanisms which drive these macroscopic behaviors is important because biofilms are ubiquitous and have important social and personal impacts.

Biofilms can have significant positive and negative impacts both personally and socially. Patients in hospitals can develop potentially lethal bacterial infections that often take the form of biofilms in their wounds. Up to 80% of surgical site infections form biofilms as discussed in [12]. Chronic sinus infections can be caused by biofilm growth in the sinus cavity [12]. Biofilm contamination of catheters and implants (such as knee replacements, artificial hearts, etc.) is dicussed in [2, 12]. In industrial

applications biofilms contaminate pipes and nozzles [22]. In [12, 33] the protective nature of the biofilm EPS is discussed. The EPS protects the suspended bacteria from what could otherwise be lethal doses of anti-bacterial or toxic treatments. In these ways and many more not mentioned biofilms cost the United States' economy billions annually and the global costs are likely in the trillions. Massol-Deyá [35] discussed one of the more positive uses of biofilms, specifically, that biofilms can be used to mitigate ground water contamination. In [23] biofilms are shown to effectively reduce soil contamination. Biofilms may be instrumental in transforming cellulose into sustainable biofuel [56] and could therefore be important for reducing green house gas emissions. The biofilms in Yellowstone look beautiful, are seen by millions of visitors every year and contribute to the income generationed by the park. Again, anywhere that there exists nutrients and water in enough abundance a biofilm can, and very likely will grow. Due to the prevalence of biofilms, understanding their growth, structural behavior and environmental impacts is fundamentally important. Mathematical modeling is a good way to increase understanding because it can allow for the prediction of mechanical values that are otherwise unmeasurable.

Biofilm modeling began in the 70s with fairly simple 1-D modeling of single species biofilms with basic kinetics [21]. The assumption that diffusivity was the only driving factor in the boundary layer was shown to be incorrect in [6] and that advection contributes to mass transport. Substrate utilization in a stream bed incorporating a reaction-diffusion equation could now be solved and that is what Williamson showed in [62]. The Sherwood number, a dimensionless number, that characterizes mass transfer, has been used in many models, e.g., [17] used the Sherwood number in their model of mass transfer to a biofilm in a stream bed. Once growth was modeled the next step was prediction of biofilm detachment. Morgenroth [36] used a detachment model to question how applicable the fundamental constant

erosion experiment is to real world systems, where backwashing often occurs, by showing that a detachment model predicts significant variation in biofilm thickness. Multi-species models that include symbiosis and competition between individuals of the same and different species were added to models with reaction-diffusion and detachment. These are called mass transfer models and [58] is one such model.

There is a class of fluid dynamic models where the biofilm is treated as a relatively high viscosity fluid in multi-dimensions. One of the difficulties of higher dimensional models is a significant increase in computation time. Additionally, fluid dynamic models require the measurement of mechanical properties, which can be difficult. This work is a fluid dynamic model and [9] presents another. Alpkvist and Klapper, [1] showed that a multispecies multidimensional continuum model could predict "finger" formations. A multidimensional, multispecies model using fluid dynamics to describe the flow over an early biomass growth model is presented in [41]. Cellular automata (CA), a.k.a, biomass based models (BbM), where biomass displaces its neighbors, shown in [42,43], was the next step in the evolution of the biofilm model. The individual based models (IbM), a.k.a., particle-based models, are the natural successors to the BbM. In IbMs the behaviors of individual bacteria, or particles, are modeled and used to predict EPS growth. In [29] Kreft showed that IbMs give rise to a more structures that have a more natural appearance, ie., rounded rather than BbM models which force spreading of EPS into a discrete grid. In [40] multiple species interactions are modeled in a multi-dimensional IbM environment. The interested reader is referred to [21] where much of this review was taken. A number of biofilm modeling review papers with different emphasis exist, infectious disease [19], multidimensions [44] and a review of biofilm ecology models [26]. Characklis and Marshall ([7]) wrote a comprehensive overview of Biofilms, their biological processes,

biofilm applications and approaches to modeling. Finally, this is by no means a complete review of the last 50 years of biofilm modeling research.

Three of the topics introduced in the biofilm model review above, fluid dynamic models for non-Newtonian fluids (a biofilm is a non-Newtonian fluid), measurement of biofilm rheological parameters for fluid dynamic models and the computational expense of obtaining solutions to these multidimensional models are immediately relavant to the model presented in this work work. If one is going to model a biofilm as a dynamic fluid it seems reasonable to ask the question,"What type of fluid is a biofilm? " Shaw ([49]) showed that biofilms have common relaxation times. Fluids with relaxation times are viscoelastic. Viscoelastic fluids are classified as non-Newtonian. In [18] a complex fluid, i.e., non-Newtonian fluid, is cheekily defined as "a fluid made up of a lot of different kinds of stuff" and while this certainly is true of a biofilm and does capture the difficulty in defining such a huge class of fluids, this definition is somewhat lacking. A more formal definition is that a non-Newtonian fluid is a fluid with a mesoscopic or "middle" length scale [18]. In this work the length scale used is 1cm and this is certainly a "middle" length. There are many phenomena associated with non-Newtonian fluids; die swell (Barus effect), rod climbing (Weissenberg effect), tubeless siphon or open siphon and self siphoning just to name a few.

Over the past 30 years a lot of effort has gone into overcoming the so-called high Weissenberg number problem (HWNP). The Weissenberg number, Wi, is defined as the product of a characteristic time and a characteristic deformation [10]. In this work the characteristic time is the relaxation time and the characteristic deformation is the velocity scale, $\mathbf{U}_0$ divided by the length scale, L_0, that is, $\mathrm{Wi} = \frac{\lambda \mathbf{U}_0}{L_0}$. Dealy [10], states that the Deborah number, De, is defined as the ratio of a characteristic time and an observation time, $\mathrm{De} = \frac{\lambda}{T_0}$. It should be noted that, in this work, $\frac{\mathbf{U}_0}{L_0} = \frac{1}{T_0}$ and so,

Wi and De are the same. In general, Wi captures the non-linearity of the a flow and De the elasticity. The exclusive use of Wi may at first seem to be a contradiction of the definitions for Wi and De. However, Dealy [10], claims that except for very small deformations or very slow flows viscoelastic fluids are highly non-linear. The HWNP has been called, by Walters [55], the "the most serious obstacle" and "infamous" in [25], problem in computational rheology.

The basic problem is that as a homogeneous viscoelastic fluid passes through a contraction, numeric models blow up and this phenomena gets worse as the grid is refined. While there is a viscoelastic fluid in this model it does not pass through a contraction. Although the Wi is used extensively in the stress model, this work does not present a HWNP and therefore these concepts will not be discussed further.

The significant issue addressed by the model in this work is maintaining the symmetry of the numeric representation of the stress tensor in a fluid dynamic biofilm model. These schemes have not been well investigated and Lee [31] asserts that as of 2003 there is only a single paper, Owens' [32], known to the authors attempting to develop such a scheme. Owens represents the elastic stress tensor, $\boldsymbol{\tau}$ as the product of a matrix $\mathbf{A}$ with its transpose. In this way the symmetry of the elastic stress tensor is enforced. Unfortunately, since $\mathbf{A}$ has no physical interpretation, this is a poor choice for a model of the elastic stress tensor. Furthermore, the symmetry of the mathematical model does not guarantee the symmetry of the numeric model [39]. The symmetry of the numeric representation of the stress tensor has been shown to be important for maintaining stability of numeric methods when describing viscoelastic flows [14]. In this case the stability is in the sense of Hadamard which is that solutions must change continuously with changes in initial conditions. Given a stable numeric model that accurately captures general viscoelastic flow the prediction of biofilm dynamics will be impacted by the ability to accurately measure rheological

parameters. Measuring these parameters is an open problem for non-Newtonian fluids in general [10]. For Newtonian fluids the Reynolds number, which depends on the viscosity of a fluid is a good dimensionless parameter for describing flow behavior. For non-Newtonian fluids which dimensionless number to use is still an open question that is often misunderstood [10]. Dealy [10], discusses the example, of a fluid with a constant elastic history. For such a fluid $\mathrm{De} = 0$ because length of observation is not inversely proportional to deformation. Further, Dealy [10], claims that " ... except in a few special cases, ..." it has not been possible to establish a general parameter which captures viscoelastic fluid behavior. However, without accurate measurement of biofilm mechanical characteristics, i.e., viscosity, relaxation time, etc., meaningful predictions, made by models, about biofilm flow behavior is limited to the anecdotal realm. In addition, measuring these values can be very difficult without damaging or destroying the biofilm specimen. Nevertheless, one must proceed with models and measurements.

The measurement of the rheological parameters of biofilms is an on going area of active research with many contributions. Shaw [49] measured relaxation times in biofilms and found that there was a commonality for the longest relaxation times of about 18 minutes. In [22] the rheological parameters of biofilms formed on the surface of drinking water production units have been measured. Viscoelastic properties of biofilms were measured by Towler [54]. Viscoelastic properties of biofilms were measured in-situ and reported in [51], in-vitro measurements were made by Rogers in [48] and measurements made using a uniaxial compression device for the work in [28].

Finally, the issue of computation time requirements has to be mentioned. Even assuming stable numeric models and accurate parameter estimation, the computation time for higher dimensional fluid flow problems can be prohibitively expensive. In

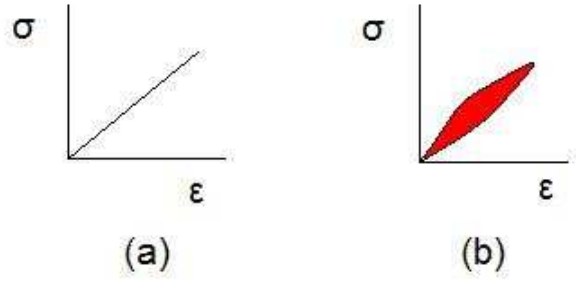
order to address the computational difficulty of determining solutions in a reasonable amount of time for the model presented in this work, it was decided to use a sparse matrix solver package called AztecOO which is a library from Trilinos. To further increase computational speed, parallel processing, a supported feature of AztecOO, has been implemented using MPI.

There is very little literature on the computational efficiency of biofilm modeling with different message passing interface schemes (OpenMP vs MPI etc) on different architectures (PC vs Mac vs Unix vs Linux) as well as CPU architectures (AMD vs Intel vs Sun) using different languages (C++, Fortran 90, Fortran 95, Matlab, Python etc) and various library solver packages of which there are many. Clearly the number of combinations is prohibitive and none of them are universally interchangeable and so comparisons are difficult to make. Furthermore, performance predictions are essentially impossible to make and a trial and error approach is more effective. For example, will a Cray super computer running 50 processors solve a problem faster than a laptop running 8 virtual processors given a model and a numeric scale? If so, then by how much will it be faster? These are open questions. The only paper found attempting to address some of these issues by Muhammad is [37], wherein, a Mickens difference scheme was applied to a mixed culture biofilm model and used to compare and contrast multicore and multiprocessor systems. A Mickens difference scheme is one that uses non-standard functions in the denominator of the employed difference scheme [5]. The results found by Muhammad are consistent with the experiences had during the computational speed testing phase for this work. While the MPI code for this work was under deveopment a consistent image of multicore/multiprocessor executions was observed. That is, when running a low complexity simulation, with an excess of processors, be they physical or virtual, computation times actually increased. What is meant by "excess" is determined by experience with an architecture, a

program and a model. This was attributed to the increase in inter-processor overhead in relation to the complexity of the computations being made. Server architecture performed significantly faster, by one to two orders of magnitude, than laptop architecture even when using the same number of processing cores, the same Ubuntu OS, C++ language and Trilinos sparse solver library AztecOO.

This work presents a 2-D, stress tensor symmetry preserving, viscoelastic fluid flow model for the purpose of capturing the flow behavior of a biofilm. The significant contribution that this work makes is the modeling of a biofilm using this symmetry preserving method. The motivation for this work are the many impacts, both positive and negative, biofilms can present economically, socially and personally. The elasticity of biofilms is well documented by experiment [27] and so should be included in fluid dynamic biofilm flow models where the elastic behavior of the biofilm has an impact on flow characteristics. See Figure 1.1 for a graphical depiction of the difference, in the response to shear, between a viscous fluid and a viscoelastic fluid. In the figure σ is the stress and ε is the strain. In (a) the stress strain curve is linear because there is no elasticity whereas in (b) there is elasticity. The elasticity is the reason for the hysteresis in the figure, because the elasticity dissipates the strain in the fluid.

Figure 1.1: A viscoelastic fluids response to shear stress [61].



Due to the ubiquitous nature of biofilms and the many potential uses and impacts of biofilms, both beneficial and detrimental, it is natural to study their behavior. It is the EPS which is modeled in this work as it is the EPS that exhibits both viscous and elastic flow behavior as discussed in the following works [22, 51, 54]. The definition for a viscoelastic fluid given on the Wikipedia page for viscoelasticity [61], begins by defining a viscous fluid as a fluid which resists shear flow linearly and an elastic material as one that strains when stressed and then returns to its original shape and then adds that a viscoelastic fluid has both properties but does not return to its original shape after the application of shear.

In this work the motion a biofilm is induced by the shear imparted onto it from the flow of a solvent as the solvent flows over the top of the biofilm. This process is recreated here mathematically by applying and then removing an inflow boundary condition. While this behavior is interesting from a mathematical perspective, as modeling it presents interesting challenges, this is not the driving motivation for the study of biofilms. It is the social and personal impacts that biofilms have which drives biofilm research.

Measuring biofilm mechanical values in vitro or in situ or in vivo is inherently difficult, [51], depending upon the mechanical value which is to be measured. Often biofilms are scraped from the surface to which they have grown, as was done in [28,48], and then rheological measures are made. Mathematical modeling is a good candidate for estimating these values without disturbing the biofilm.

Unfortunately, mathematical modeling of viscoelastic fluids (and non-Newtonian fluids in general) has often proven to be extremely difficult. One method for developing models is to make macroscopic assumptions about the fluid and devise constitutive equations governing mass balance, momentum and energy. In this way the flow characteristics of the bacterial colony generated EPS can be approximated.

One common model, and what is used in this work, is the Navier-Stokes equation. The motivation for the use of the Navier-Stokes equation is presented in Chapter 2. Dupret [14] showed that the preservation of the symmetry of the numeric representation of the stress tensor has been shown to be critical for maintaining the stability of numeric methods. To this end, a novel viscoelastic fluid model that preserves the symmetry of the numeric stress tensor has been developed. Dr. Lee's work [30, 31] is used as a primary source for the mathematics of the symmetry preserving scheme. The noteworthy deviation from [30,31] is the inclusion of a second viscous fluid as apposed to a single uniform viscoelastic fluid. This second, purely viscous, fluid flows over and around the viscoelastic biofilm. This is not unlike the experimental situation where a biofilm is grown with a nutrient flowing over the top of it. In Chapter 2 the mathematics which recreates this scenario is developed and in Chapter 4 the simulated behavior is illustrated.

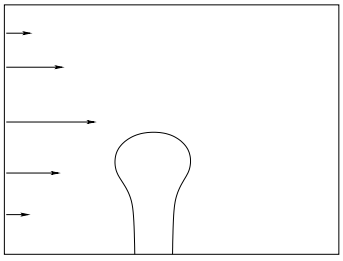
The relaxation time of a viscoelastic fluid is the amount of time it takes for the fluid to recover once a shear stress has been removed. In a biofilm the relaxation time is related to the elastic stress. In this model, the elastic stress is caused by a shear stress which is in turn caused by the flow of a solvent over the top of the biofilm. In [27] it is shown that biofilms exhibit viscoelastic behavior, specifically, that biofilms have relaxation times, a defining characteristic of viscoelastic flow.

A typical experimental setup is to grow a biofilm under different nutrient flow conditions. Various flow conditions have been shown to produce variations in biofilm structures with streamers forming under high flow and mushroom like structures in low flow [19]. A phenotype response to flow conditions is associated with these structures ([20]) and attributed to an evolutionary trait in [49]. Regardless of the mechanism that produces these variations in biofilm structures, low flow tends to produce fluffy biofilms where as high flow is ascribed to more dense biofilms. Once a

biofilm has been grown the nutrient flow can be varied and the reaction of the biofilm to this flow can measured. It is with this typical experimental setup in mind that the model in this work was developed.

In this work the initial state of the biofilm is assigned a shape and the resulting deformation is captured. The initial velocities, horizontal and vertical, of the solvent and the biofilm volume fraction are set equal to zero everywhere in the modeled domain. The inlet boundary conditions induce flow throughout the modeled domain. The solvent flow provides the mechanical shear stress which induces flow in the biofilm. The inlet flow is set to zero after a period of time and the simulation is terminated after the velocity reaches quasi-equilibrium. It is reasonable to consider allowing the flow velocity to reach equilibrium because the longest elastic response time for biofilms is on the order 18 minutes [49], which far exceeds the time it takes for the solvent to reach a quasi-equilibrium state. While a biofilm is composed of living organisms and does grow over time, due to the time scale of the model under consideration here and the much longer time scale associated with biofilm growth, growth has not been included in this model. Since the growth of the biofilm is not considered, the consumption of nutrients from the solvent is ignored.

Figure 1.2: A schematic figure of the model domain and biofilm profile.



The domain of the model is a 2D square of side length 1cm. The case where a biofilm is located on the inside and the bottom of this domain is considered, see Figure

1.2. This scale is applicable to a typical adult Foley catheter, in which [12] showed they have grown. The modeled domain could be viewed as a 1cm long, vertical cross section of such a catheter with a small biofilm attached to the bottom. Within the square domain, motion of various initial biofilm profiles subjected to external flow are considered. The purpose is to determine the flow characteristics of the fluids in a pipe with an emphasis on the viscoelastic behavior of the attached biofilm. A time scale of 1 minute is used because, once again, the longest relaxation times for biofilms has been shown to be consistently around 18 minutes [49].

Stress in a biofilm is modeled by the stress tensor and there are several papers addressing the issue of the importance of maintaining the positive definiteness of the stress tensor when modeling viscoelastic flow. Dupret [14] showed that the loss of the positive definiteness of the stress tensor yields "physically meaningless equations" and that the effects of errors are minimized by using the Oldroyd-B stress model originally developed by Oldroyd in [38]. Fattal used a change of variables from the stress $\boldsymbol{\tau}$ to $ln(\boldsymbol{\tau})$. The purpose of this transformation was to capture the changes in stress associated with flow of a viscoelastic fluid through a contraction for high Weissenberg numbers. The purpose of this change of coordinates is that changes in the stress, for viscoelastic fluids flowing through a contraction, grow exponentially and so a polynomial basis function will fail to capture them. Hence the use of the natural log to reduce the rate of change to an amount, that a polynomial can describe, and thereby expand stability for numeric methods in the regime of the HWNP.

Numerical methods which describe viscoelastic fluid flow are sensitive to asymmetries in the numeric representation of the stress tensor. The model which is at the heart of our work emphasizes the development of a new method which forces the numeric solution of the stress tensor to be symmetric. Lee [30, 31] accomplished this by showing that the elastic stress differential equation can be rewritten in the

form of a symmetric matrix Riccati differential equation (SMRDE) and then showing that the numeric solution to the SMERD is always symmetric. Hence, the numeric representation of the stress tensor is symmetric.

In this work, there is an important distinction between the rheological values for a biofilm and the parameter values used for modeling a biofilm. For example, in [27] the viscosity of a biofilm is measured using a saturated biofilm. This is a necessity because a dehydrated biofilm is little more than dust. The relaxation time and the viscosity of a biofilm are reported as single values, in this work, they are functions of biofilm concentration. That is, these values are scaled by the biofilm volume fraction. The effect of this is that these intrinsic biofilm parameters are diminished linearly as the volume fraction of biofilm goes to zero. Since, the parameters for different biofilm volume fractions are not fully known, this process is as accurate a method as can be determined at this time.

In this thesis, the mathematical description of the viscoelastic flow of a biofilm using partial differential equations is presented first. The stability of the numeric method is maintained through a development related to the SMRDE. As a direct result the numeric representation, of the second order stress tensor, is always symmetric. The foundation of this method is developed, in part, as it pertains to an important discussion associated with a variation to the stress partial differential equation from the one used in [30, 31]. This variation has only a theoretical impact on the numeric solution developed by Lee in [30, 31] but no substantial changes are required.

The Navier-Stokes equation (2.3) can be solved in one of two ways. One option is to use the purely Lagrangian representation of the total derivative (2.25) which is known as the method of characteristics [31]. However, this method distorts grid points which then leads to errors over time [3, 31]. An alternative, and the method

used in this work, is the so-called Eulerian-Lagrangian method (ELM) [13, 31, 45]. In [45] Pironneau describes each time step of the ELM process as a Stokes problem with the previous solution moving along a characteristic. A Stokes problem is the linearization of the steady Navier-Stokes equation [60]. The ELM requires solving for the characteristic feet, known as the departure feet. The departure feet are described in [31] as the positions of particles, in the past, that are, in the present, located at points of interest.

The Taylor-Hood elements are used to maintain stability as required by the so-called Inf-Sup condition as detailed in [52] and developed for discrete solutions in [16]. For this work quadratic elements have been selected for capturing the velocity dynamics. The consequence of the Inf-Sup condition is that linear elements must be used to model the pressure. While the presented system of coupled DEs is radically different from the DEs considered in the development of the Inf-Sup condition, it is assumed that the requirements for stability still apply.

In this work the advection diffusion equation for the biofilm volume fraction is stabilized by the Galerkin least squares (GLS) method. The GLS method does well with advection dominate systems [46]. The system modeled in this work is advection dominant through the middle of the domain. This advection dominance transitions to diffusion dominance on the top and bottom of the domain where the velocity is zero due to non-slip boundary conditions. It is assumed that this transition does not impact the stability of the GLS method. Before the GLS method is discussed a brief overview of its development is presented, beginning with the Galerkin method. The Galerkin methods introduces negative numeric diffusion [11]. The compensation for this negative numeric diffusion is called the Petrov Galerkin method which uses upwinding to compensate for the deficiency in the Galerkin method. Upwinding is used because it is equivalent to numeric diffusion [11]. The problem with the

Petrov Galerkin method is that the introduced diffusion can occur transversely to the direction of flow in higher dimensional flow problems [11]. This causes excess diffusion in higher dimensional problems. The solution for this is the so-called streamlined upwind Petrov Galerkin, (SUPG), method. In SUPG the upwinding is performed only in the direction of flow as discussed in [4]. The issue with SUPG is that the introduced stabilization term is not symmetric [11]. This lack of symmetry affects the ability to determine the stability of the method [11]. The GLS method term is symmetric and this is called ," ... a strong point." in [47] as well as noting that the GLS method actually solves the least squares problem, i.e., by minimizing the residual error. It should be noted that in 1D, with linear elements SUPG and GLS are identical [11]. The exact form of the GLS method employed in this work is presented in Chapter 3. The sub grid scale method, (SGS) corrects for the remaining errors in the GLS method for reaction dominate systems [11]. Since the presented model is not reaction dominant as it contains no modeled reactions, the SGS method has not been used.

Thesis Organization:

The discussion in this thesis the chapters proceed as follows,

In **Chapter 2** the model is motivated and then described. A detailed description of the stress model development is presented.

In **Chapter 3** the numeric representation of the model, presented in Chapter 2, is developed.

In **Chapter 4** the results of the numeric model are presented.

MODEL OF BIOFILM AS VISCOELASTIC FLUID

In this chapter the mathematical description of a novel viscoelastic biofilm flow model is introduced. The model captures the second order elastic stress tensor for the the biofilm. The pressure, horizontal and vertical velocities for two fluids, one viscous water and the other viscoelastic biofilm are modeled. In addition, the advection of the biofilm is described. The model section begins with listing the complete system of coupled partial differential equations that models water flowing over a biofilm. Afterwards each partial differential equation is discussed in detail. In addition, a brief development of the stress model is presented.

The motivation for the use of the Navier-Stokes equation stems from the need to describe the momentum of the biofilm and surrounding bulk fluid. The fact that there is no change in the mass of the system over time, coupled with the incompressibility condition, $\nabla \cdot \mathbf{u} = 0$, a fundamental assumption, means that there is no change in the density of the modeled fluids. In this work the fluids are considered to be isothermal and so the energy for the system does not need to modeled. The Navier-Stokes equation comes from balancing the linear momentum of the system, that is,

$$\frac{\partial}{\partial t} \int_{\Omega} \mathbf{u} d\mathbf{x} = \int_{\partial\Omega} \mathbf{C} \cdot \mathbf{n} ds, \tag{2.1}$$

where $\mathbf{u}$ is the velocity, t is the time, Ω is the domain, $\mathbf{x}$ is the spacial variable, $\partial\Omega$ is the boundary of the domain, $\mathbf{C}$ is the so called Cauchy stress tensor, $\mathbf{n}$ is the outward pointing unit normal and s is the scalar surface area of the boundary. The Cauchy stress tensor is defined as $\mathbf{C} = -p\mathbf{I} + \mathbf{T}$, where p is the pressure, $\mathbf{I}$ is the 2X2 identity tensor and $\mathbf{T}$ is the total stress. Another fundamental assumption is that the total stress can be rewritten as the sum of the viscous and elastic stress, i.e.,

$\mathbf{T} = 2\eta_0 D(\mathbf{u}) + \boldsymbol{\tau}$, where η_0 is the total viscosity defined by equation (2.8) below, $D(\mathbf{u})$ is the strain rate tensor and $\boldsymbol{\tau}$ is the elastic stress tensor.

Model:

The modeled system is composed of water and biofilm flowing through a 1 cm by 1 cm domain. The water is a viscous fluid and the biofilm is a viscoelastic fluid. The volume fraction is used to describe the biofilm. The velocity and pressure of the flow is captured by the Navier-Stokes equation and the incompressibility condition. In this work the elastic stress can be described by various DEs from a class of DEs. The criteria for a class member is that it can be rewritten as a Lie derivative. The biofilm volume fraction is given by the advection equation.

Viscoelastic Fluid:

A viscoelastic fluid is a fluid that displays both viscous and elastic properties. A biofilm has demonstrated viscoelastic properties [27]. The molecular polymers which make up the EPS are interlinked but can flow over and around each other. In this work the viscoelastic deformation of the biofilm volume fraction, caused by external flow, is modeled.

The non-dimensional system of coupled partial differential equations which makes up the model is listed below. The nomenclature for the system is listed in Table 2.1 after the system of PDEs. The system is presented in the order in which the DEs are solved. This is discussed in more detail in Chapter 3.

The classic Navier-Stokes equation (NSE), (2.2) is the starting off point for the modified NSE used in this work.

$$\rho\left(\frac{\partial \mathbf{u}}{\partial t}+\mathbf{u}\nabla\mathbf{u}\right)=-\nabla p+\nabla\cdot\mathbf{T}, \tag{2.2}$$

where $\mathbf{u}$ is the velocity, ρ is the density, p is the pressure and $\mathbf{T}$ is the total stress tensor. The total stress $\mathbf{T}$ is assumed to be the sum of the viscous stress $2\left[\left(1+\left(\frac{\eta_p}{\eta_s}-1\right)\varphi\right)D(\mathbf{u})\right]$ and the elastic stress $\varphi\boldsymbol{\tau}$, where η_s and η_p are the viscosities of the solvent and polymer respectively and $D(\mathbf{u})$ is the strain rate tensor. The strain rate tensor is the symmetric part of the gradient of the flow field, $D(\mathbf{u})=\frac{1}{2}(\nabla\mathbf{u}+\nabla\mathbf{u}^T)$. The biofilm volume fraction has been assigned the variable φ.

The Navier-Stokes equation states that the total derivative of the velocity and the divergence of the Cauchy stress tensor are equal due to momentum balance. The Cauchy stress tensor is a 2nd order tensor separated into two terms, the pressure tensor and the stress tensor. The non-linear term $\mathbf{u}\nabla\mathbf{u}$ will be discarded because the magnitude of its components are small. In Chapter 4 the surfaces of the components of $\mathbf{u}\nabla\mathbf{u}$ are shown to have small magnitudes. All body forces have been removed by assuming that the motion of the modeled domain is not changing, i.e., there are no externally imposed changes in momentum.

The modified and non-dimensional Navier-Stokes equation:

$$\mathrm{Re}_s\frac{\partial \mathbf{u}}{\partial t}=2\nabla\cdot\left[\left(1+\left(\frac{\eta_p}{\eta_s}-1\right)\varphi\right)D(\mathbf{u})\right]-\nabla p+\nabla\cdot(\varphi\boldsymbol{\tau})\,. \tag{2.3}$$

The Reynolds number for the solvent, Re_s, is used and is described by the following,

$$\mathrm{Re}_s = \frac{\rho U_0 L_0}{\eta_s}, \tag{2.4}$$

where η_s is the solvent viscosity and $U_0 = L_0/T_0$ with L_0 and T_0 are the characteristic velocity, length and time scales respectively.

Incompressibility condition:

$$\nabla \cdot \mathbf{u} = 0. \tag{2.5}$$

Stress constitutive equation:

$$\varphi \mathcal{L}_{\mathbf{u},\nabla\mathbf{u}}\mathbf{c} + \alpha \mathbf{c} = \beta \mathbf{I}, \tag{2.6}$$

where the so called conformation stress is denoted by $\mathbf{c}$ out of respect for Dr. Lee who used this notation in his work [30, 31].

Advection equation:

$$\frac{\partial \varphi}{\partial t} + \mathbf{u} \cdot \nabla \varphi = 0. \tag{2.7}$$

The advection equation captures the evolution of the biofilm volume fraction under the flow field $\mathbf{u}$.

Navier-Stokes Equation:

Here the fundamental assumption is that the total stress can be written as the sum of the viscous and elastic stresses, $\mathbf{T} = 2\eta_0 D(\mathbf{u}) + \varphi\boldsymbol{\tau}$, where η_0 is the total viscosity (2.8). One should note that since the macroscopic fluid is a linear combination of two fluids, a viscous solvent and a viscoelastic polymer (water and EPS respectively), there is not a single constant which could be called a Reynolds

Nomenclature	
Symbol	Name
$\mathbf{u}$	Velocity Vector
t	Time
ρ	Water & Biofilm Density
Re_s	Solvent Reynolds Number
η_s	Solvent Viscosity
η_p	Polymer Viscosity
φ	Polymer Volume Faction
p	Pressure
$\boldsymbol{\tau}$	Stress Tensor
$\mathcal{L}$	Lie Derivative
$\mathbf{c}$	Conformation Stress Tensor
α, β	Lie Derivative Constants
$\mathbf{x}$	Spatial position
L_0	Characteristic Length
T_0	Characteristic Time
U_0	Characteristic Speed

Table 2.1: Model Nomenclature

number. However, the viscosity of water is used as a non-dimensionalizing constant and so the Reynolds number for water is the value by which the modified Navier-Stokes equation has been scaled.

Often Navier-Stokes problems have a single constant viscosity, this is not the case here. In this work it is assumed that the viscosity is a linear combination of two viscosities, specifically,

$$\eta_0 = \eta_s(1-\varphi) + \eta_p\varphi, \tag{2.8}$$

where φ is the volume fraction of polymer and η_s and η_p are the viscosities of the solvent and polymer respectively and η_0 is, effectively, the viscosity used in this model. It should be noted that (2.8) is scaled by the solvent Reynolds number, Re_s, to arrive at the term in the modified NSE (2.3). This scaling is so that the solvent viscosity can be used as a non-dimensionalizing scalar. Since the Reynolds number, in this

model, is not constant the normal method of scaling the pressure and stress terms by the Reynolds number and subsequently, passing it through the derivatives, is not mathematically valid. In this case the NSE (2.3) is scaled by the Reynolds number for the solvent water, Re_s. Lastly, the elastic stress tensor is scaled by the volume fraction of the polymer. In this way the elastic stress doesn't exist where there is no polymer. In addtion, by using this scheme the actual viscosity of a biofilm need not be known, since all that is required is the ratio of biofilm viscosity to water viscosity. For most of the results in Chapter 4 a 500:1 ratio has been used. After applying all of these considerations we arrived at the equation (2.3). The incompressibility condition, the development of the elastic stress PDE and the advection DE are discussed in turn next.

Incompressibility:

It is assumed that the fluids are incompressible as expressed by (2.5). Typically one of the consequences of this assumption is that the divergence of the second half of the strain rate tensor is zero, i.e., $\nabla \cdot (\nabla \mathbf{u})^T = 0$. However, since our effective viscosity η_0 is not constant, the $(\nabla \mathbf{u})^T$ term is persistent. Next the partial differential equation (2.6) for the stress is developed.

Stress:

The scaling of the the lie derivative, $\mathcal{L}_{\mathbf{u},\nabla\mathbf{u}}$ by φ is a variation to the system of differential equations proposed in [30,31]. This variation introduces a subtlety to the solution developed in [30, 31] that must be mentioned. However, before the effects of this variation, and the resulting modification to the numeric solution in [30, 31] is presented, the original work is developed, in the next section in part, to explain both the original solution and why this variation is indeed a subtle complication.

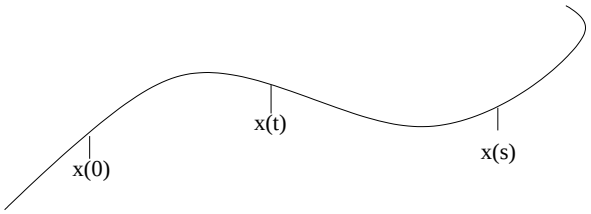
Stress Development: The development of the solution in [30, 31] begins with a general discussion of flow fields. Given a flow field as in Figure 2.1, the Lagrangian and Eulerian frames can be described. The Eulerian coordinate description uses a coordinate frame fixed in space and is the reference frame used in this work. In general, the Eulerian frame need not be the reference frame [11]. The Lagrangian coordinate frame moves with a parcel of fluid. The symbolic assignments that give this discussion mathematical meaning will now be introduced. Let $\mathbf{x}(t)$ be the Eulerian position with an initial point, $\mathbf{x}(0) = \mathbf{x}_0$, in the flow field given by the velocity, $\mathbf{u}(\mathbf{x}(t), t)$. Then the Lagrangian flow field can given by first describing how the Lagrangian particle positions $\mathbf{X}$ are related to the Eulerian position $\mathbf{x}$, specifically,

$$\mathbf{X} = \mathbf{X}(\mathbf{x}_0, t). \tag{2.9}$$

The resulting flow field is

$$\frac{\partial \mathbf{X}(\mathbf{x}_0, t)}{\partial t} = \mathbf{u}(\mathbf{X}(\mathbf{x}_0, t), t). \tag{2.10}$$

Figure 2.1: A flow line with an initial condition and two future positions.



It is possible to generalize further by noting that the initial time need not be zero, that is, given initial position x and initial time t, define $\mathbf{X}(\mathbf{x}, t; s)$ for some time s and where $\mathbf{X}(\mathbf{x}, t; t) = \mathbf{x}$. Note that s need not be greater than t and when $s < t$

the point is moving backwards in time. Not only is movement backwards in time along flow lines allowed but it isnecessary.

Now for the more general Lagrangian case, the connection between the Lagrangian position and its flow field is,

$$\frac{\partial \mathbf{X}(\mathbf{x}, t; s)}{\partial s} = \mathbf{u}(\mathbf{X}(\mathbf{x}, t; s), s). \tag{2.11}$$

The concept that matters here is the deformation of the Lagrangian particle positions. Let $\mathbf{F}$ be this deformation. This deformation occurs along flow lines and should observe certain properties. The deformation from a point on a flow line should be a continuous process that can move forward and backwards in time from and through that point. More formally, let $F(\mathbf{x}, t; t_0, t_1)$ be the deformation with initial point in the flow field $(\mathbf{x}, t)$ moving along a flow line from time t_0 to t_1. The deformation from t_0 to t_1 followed by the deformation from t_1 to t_2 should be the deformation from t_0 to t_2. This is stated mathematically as, $\mathbf{F}(\mathbf{x}, t; t_0, t_1)\mathbf{F}(\mathbf{x}, t; t_1, t_2) = \mathbf{F}(\mathbf{x}, t; t_0, t_2)$. The immediate assumption is that $t_0 < t_1 < t_2$ but, again, this need not be the case and the backwards in time flow is not just an interesting idea but fundamental to the numeric solution of the Lie derivative. The definition of the relative deformation gradient is dependent upon the stress model. The stress model depends on the objective rate. The names of different stress models are listed next to their associated objective rates in Table 2.2.

Objective Rate & the Rate of Strain	
Objective Rate	Rate of Strain
$\nabla \mathbf{u}$	Upper Convected Maxwell [31]
$-\nabla \mathbf{u}^T$	Lower Convected Maxwell [31]
$\frac{a+1}{2}\nabla \mathbf{u} + \frac{a-1}{2}\nabla \mathbf{u}^T$ [24]	Gordon-Schowalter

Table 2.2: Characteristic Deformation

The relative deformation gradient is developed next. Consider the deformation along a flow line with initial position and time $(\mathbf{x}, t)$, where the deformation starting at t_1 towards t_2, where $t_2 > t_1$. Then the forward in time deformation is denoted, $\mathbf{F}(\mathbf{x}, t; t_1, t_2)$ and must be equal to the gradient at position t_1 of the flow starting at t_1 moving in time towards t_2, that is,

$$\mathbf{F}(\mathbf{x}, t; t_1, t_2) = \nabla_{\mathbf{z}} \mathbf{X}(\mathbf{z}, t_1; t_2), \tag{2.12}$$

where $\mathbf{z} = \mathbf{X}(\mathbf{x}, t; t_1)$, is the position of the parcel of fluid at t_1 that started life at position and time $(\mathbf{x}, t)$. Note that the subscript $\mathbf{z}$ on the ∇ means that the del operator is with respect to $\mathbf{z}$. Note, if $t_1 = t$ then $\mathbf{z} = \mathbf{x}$ and $\mathbf{F}(\mathbf{x}, t; t, t_2) = \nabla_{\mathbf{x}} \mathbf{X}(\mathbf{x}, t; t_2) = \nabla \mathbf{X}(\mathbf{x}, t; t_2)$. The argument presented in [30, 31] is to assume that $\mathbf{X}$ is a diffeomorphism and hence is 'smooth' enough to allow for the interchange of limits. This interchange is used after applying a partial derivative to (2.12) with respect to time as follows next,

$$\begin{aligned} \frac{\partial \mathbf{F}(\mathbf{x}, t; t_1, t_2)}{\partial t_2} &= \frac{\partial \nabla_{\mathbf{z}} \mathbf{X}(\mathbf{z}, t_1; t_2)}{\partial t_2} \\ &= \nabla_{\mathbf{z}} \frac{\partial \mathbf{X}}{\partial t_2}. \end{aligned} \tag{2.13}$$

Now apply equation (2.11) to obtain

$$\frac{\partial \mathbf{F}(\mathbf{x}, t; t_1, t_2)}{\partial t_2} = \nabla_{\mathbf{z}} \mathbf{u}(\mathbf{X}(\mathbf{z}, t_1; t_2), t_2). \tag{2.14}$$

Next change the coordinates of the gradient from $\mathbf{z}$ to $\mathbf{x}$ by use of the definition of the relative deformation gradient (2.12) and the chain rule

$$\frac{\partial \mathbf{F}(\mathbf{x}, t; t_1, t_2)}{\partial t_2} = \nabla \mathbf{u}(\mathbf{X}(\mathbf{x}, t; t_2), t_2)\mathbf{F}(\mathbf{x}, t; t_1, t_2). \tag{2.15}$$

Equation (2.15) states that the change in the relative deformation gradient with respect to time, is the deformation of the gradient of the velocity field deformed towards t_2 with the initial condition $\mathbf{F}(\mathbf{x}, t; t_1, t_1) = \mathbf{I}$, where $\mathbf{I}$ is the identity tensor. A differential equation in the form of (2.15) is solved numerically in Chapter 3, in a more general setting, and used in the numeric solution to the stress PDE. The form of equation (2.15) is critical to the numeric solution of the elastic stress partial differential equation. In addition, (2.15) is a fundamental component of the general solution to the Riccati differential equation.

Since the fluid is incompressible the determinant of the deformation $\mathbf{F}$ must be one, that is, $\det\mathbf{F} = 1$ [8]. Therefore $\mathbf{F}$ is invertible and $\mathbf{F}^{-1}$ is simply the deformation backwards in time, where $t_2 > t_1$. Note, the product of the forward and backward deformation should be the identity, i.e.,

$$\mathbf{F}(\mathbf{x}, t; t_1, t_2)\mathbf{F}(\mathbf{x}, t; t_2, t_1) = \mathbf{I}. \tag{2.16}$$

In order to determine the derivative of the backwards deformation, use (2.12), and apply the product rule to (2.16),

$$0 = \frac{\partial \mathbf{F}(\mathbf{x}, t; t_1, t_2)\mathbf{F}(\mathbf{x}, t; t_2, t_1)}{\partial t_2} \tag{2.17}$$

$$= \frac{\partial \mathbf{F}(\mathbf{x}, t; t_1, t_2)}{\partial t_2}\mathbf{F}(\mathbf{x}, t; t_2, t_1) + \mathbf{F}(\mathbf{x}, t; t_1, t_2)\frac{\partial \mathbf{F}(\mathbf{x}, t; t_2, t_1)}{\partial t_2} \tag{2.18}$$

$$= \nabla \mathbf{u}(\mathbf{X}(\mathbf{x}, t; t_2), t_2) + \mathbf{F}(\mathbf{x}, t; t_1, t_2)\frac{\partial \mathbf{F}(\mathbf{x}, t; t_2, t_1)}{\partial t_2}, \tag{2.19}$$

and gives the differential equation for the backwards deformation gradient,

$$\begin{aligned}\frac{\partial \mathbf{F}(\mathbf{x},t;t_2,t_1)}{\partial t_2} &= -\mathbf{F}(\mathbf{x},t;t_1,t_2)^{-1}\nabla\mathbf{u}(\mathbf{X}(\mathbf{x},t;t_2),t_2) \\ &= -\mathbf{F}(\mathbf{x},t;t_2,t_1)\nabla\mathbf{u}(\mathbf{X}(\mathbf{x},t;t_2),t_2), \end{aligned} \tag{2.20}$$

with initial condition $\mathbf{F}(\mathbf{x},t;t_1,t_1)=\mathbf{I}$. This result is required for the solution to the Lie derivative representation of the stress PDE. The equations (2.15) and (2.20) are two components that will be used to show that the Lie derivative is of the form of the Oldroyd-B stress model. Now, consider a generalization of (2.15), beginning with the transition matrix $\mathbf{L}$ that satisfies the differential equation,

$$\frac{\partial \mathbf{L}(\mathbf{x},t;t_1,t_2)}{\partial t_2} = \Phi(\mathbf{X}(\mathbf{x},t;t_2),t_2)\mathbf{L}(\mathbf{x},t;t_1,t_2), \tag{2.21}$$

with initial condition $\mathbf{L}(\mathbf{x},t;t_1,t_1)=\mathbf{I}$, where Φ is some objective rate.

Similarly, define the derivative of the backwards in time transition matrix $\mathbf{L}(\mathbf{x},t;t_2,t_1)$, where here again $t_1<t_2$,

$$\frac{\partial \mathbf{L}(\mathbf{x},t;t_2,t_1)}{\partial t_2} = -\mathbf{L}(\mathbf{x},t;t_2,t_1)\Phi(\mathbf{X}(\mathbf{x},t;t_2),t_2), \tag{2.22}$$

with initial condition $\mathbf{L}(\mathbf{x},t;t_2,t_2)=\mathbf{I}$.

In Chapter 3 the numeric approximation to (2.21) is used in conjunction with the numeric solution to the generalized Lie derivative to numerically solve the stress partial differential equation (2.6). Before the generalized lie derivative is developed a short digression is made to define the total derivative as it is an important part of the Lie derivative.

Given any function, $\mathbf{f}(\mathbf{x},t)$ with Lagrangian coordinates $\mathbf{X}(\mathbf{x},t;t)=\mathbf{x}$, where the time t in both frames is the same. Then the following must hold,

$$\mathbf{f}(\mathbf{x},t)=\mathbf{f}(\mathbf{X}(\mathbf{x}),t)=\mathbf{F}(\mathbf{X},t), \tag{2.23}$$

and after taking the gradient and using the chain rule,

$$\begin{bmatrix} \frac{\partial F}{\partial \mathbf{X}} & \frac{\partial F}{\partial \mathbf{t}} \end{bmatrix} = \begin{bmatrix} \frac{\partial f}{\partial \mathbf{x}} & \frac{\partial f}{\partial \mathbf{t}} \end{bmatrix} \begin{bmatrix} \frac{\partial \mathbf{x}}{\partial \mathbf{X}} & \frac{\partial \mathbf{x}}{\partial \mathbf{t}} \\ \frac{\partial \mathbf{t}}{\partial \mathbf{X}} & \frac{\partial \mathbf{t}}{\partial \mathbf{t}} \end{bmatrix} = \begin{bmatrix} \frac{\partial f}{\partial \mathbf{x}} & \frac{\partial f}{\partial \mathbf{t}} \end{bmatrix} \begin{bmatrix} \frac{\partial \mathbf{x}}{\partial \mathbf{X}} & \mathbf{v} \\ \mathbf{0} & 1 \end{bmatrix}. \tag{2.24}$$

In [11] the second equation from the second product in 2.24 is the well known relationship between Lagrangian and Eulerian frames, the so called total derivative,

$$\frac{D\mathbf{F}(\mathbf{x},t)}{Dt}=\frac{D\mathbf{f}(\mathbf{x},t)}{Dt}=\left.\frac{\partial \mathbf{f}\left(\mathbf{X}(\mathbf{x},t;s)\right)}{\partial s}\right|_{s=t}=\mathbf{f}_t+\mathbf{v}\cdot\nabla\mathbf{f}. \tag{2.25}$$

The expression on the left hand side of (2.25) is in the Lagrangian frame and the right hand side is in the Eulerian frame.

Next the Lie derivative is developed. It can be shown that the Lie derivative in the Stress constitutive equation (2.6) is equivalent to the following equation,

$$\mathcal{L}_{\mathbf{v},\mathbf{L}}\boldsymbol{\zeta}(t):=\mathbf{L}(t;t,s)\left.\frac{D\left(\mathbf{L}(t;s,t)\,\boldsymbol{\zeta}(s,t)\,\mathbf{L}(t;s,t)^T\right)}{Ds}\mathbf{L}(t;t,s)^T\right|_{s=t}, \tag{2.26}$$

where $\mathbf{L}(t;s,s)=I$ and $t<s$. It must be noted that (2.26) is a derivative in the Lagrangian frame and yet another form of the generalized Lie derivative. In fact, all objective rates of second order tensors are Lie derivatives [34]. The specific form of the Lie derivative used in equation (2.26) is known as the Truesdell stress rate and is the Lie derivative of the so called Kirchhoff stress tensor [50].

Think of the $\mathbf{L}(t;t,s)$ function as a change in the dynamic system from t to s. Then, $\mathbf{L}(t;t,s)\mathbf{L}(t;s,t) = \mathbf{I}$, which is the same as $\mathbf{L}(t;t,s) = \mathbf{L}(t;s,t)^{-1}$ and $\mathbf{L}(t;t,s)^{-1} = \mathbf{L}(t;s,t)$ and should be interpreted to mean that the product is equivalent to no change in the system, that changes are locally linearizable, invertible (because incompressibility guarantees that $\det(\mathbf{L}) \neq 0$) and that this is true for both directions of flow in time.

Applying the product rule to the derivative in (2.26) yields the following,

$$\begin{aligned}\mathcal{L}_{\mathbf{v},\mathbf{L}}\boldsymbol{\zeta}(t) =& \mathbf{L}(t;t,s)\frac{D\mathbf{L}(t;s,t)}{Ds}\boldsymbol{\zeta}(s,t)\mathbf{L}(t;s,t)^T\mathbf{L}(t;t,s)^T\Big|_{s=t} \\ &+ \mathbf{L}(t;t,s)\mathbf{L}(t;s,t)\frac{D\boldsymbol{\zeta}(s,t)}{Ds}\mathbf{L}(t;s,t)^T\mathbf{L}(t;t,s)^T\Big|_{s=t} \\ &+ \mathbf{L}(t;t,s)\mathbf{L}(t;s,t)\boldsymbol{\zeta}(s,t)\frac{D\mathbf{L}(t;s,t)^T}{Ds}\mathbf{L}(t;t,s)^T\Big|_{s=t}. \end{aligned} \tag{2.27}$$

There are three terms in 2.27. The first term requires the forward in time equation 2.21 to simplify and becomes the second term in 2.28. The third term requires the backwards in time equation 2.22 to simplify and becomes the third term in 2.28. The middle term uses 2.16 to simplify and becomes the total derivative in 2.28.

$$\frac{D\boldsymbol{\zeta}(s,t)}{Ds} + \boldsymbol{\Phi}\boldsymbol{\zeta}(t,t) - \boldsymbol{\zeta}(t,t)\boldsymbol{\Phi}^T\Big|_{s=t}. \tag{2.28}$$

The generalized Lie derivative, denoted $\mathcal{L}_{\mathbf{v},\boldsymbol{\Phi}}\boldsymbol{\zeta}(t)$, is defined as,

$$\mathcal{L}_{\mathbf{v},\boldsymbol{\Phi}}\boldsymbol{\zeta}(t) = \frac{D\boldsymbol{\zeta}(t)}{Dt} - \boldsymbol{\Phi}(t)\boldsymbol{\zeta}(t) - \boldsymbol{\zeta}(t)\boldsymbol{\Phi}(t)^T, \tag{2.29}$$

where $\boldsymbol{\zeta}$ is a second order tensor, $\frac{D\cdot}{Dt}$ is the total derivative, $\mathbf{v}$ is the flow field and $\boldsymbol{\Phi}$ is some objective rate.

Then for the stress tensor $\boldsymbol{\tau}$, the velocity field $\mathbf{u}$ and with the objective rate $\nabla\mathbf{u}$ the Lie derivative becomes,

$$\mathcal{L}_{\mathbf{u},\nabla\mathbf{u}}\boldsymbol{\tau} = \frac{D\boldsymbol{\tau}(t)}{Dt} - \nabla\mathbf{u}(t)\,\boldsymbol{\tau}(t) - \boldsymbol{\tau}(t)\,\nabla\mathbf{u}(t)^T. \tag{2.30}$$

Equation (2.30) is obtained by letting $\boldsymbol{\Phi} = \nabla\mathbf{u}$ in (2.29) and expressing the total derivative using its definition (2.25) the Lie derivative turns into the so-called Upper Convected Maxwell Derivative (UCMD) or more simply the Upper Convected Derivative (UCD). The UCD is at the heart of the Oldroyd-B stress model which is used for many of the results presented in Chapter 4 as well as the vehicle for drawing the connection between the Lie derivative and the symmetric matrix Riccati differential equation (SMRDE).

Next, let $\boldsymbol{\Phi} = -\nabla\mathbf{u}^T$, then the Lie derivative becomes what is known as the lower convected derivative.

$$\mathcal{L}_{\mathbf{u},-\nabla\mathbf{u}^T}\boldsymbol{\tau} = \frac{\partial\boldsymbol{\tau}}{\partial t} + \mathbf{u}\nabla\boldsymbol{\tau} + \nabla\mathbf{u}^T\boldsymbol{\tau} + \boldsymbol{\tau}\nabla\mathbf{u}, \tag{2.31}$$

where $\frac{D\boldsymbol{\tau}(t)}{Dt} = \frac{\partial\boldsymbol{\tau}(t)}{\partial t} + \mathbf{u}\nabla\boldsymbol{\tau}$ is the total derivative defined by equation (2.25). This form of stress model is not used.

The Johnson-Segalman objective rate, defined in [24], becomes the Gordon-Schowalter derivative by letting $\boldsymbol{\Phi} = \frac{a+1}{2}\nabla\mathbf{u} + \frac{a-1}{2}\nabla\mathbf{u}^T$, where $a \in [-1, 1]$, in the Lie derivative,

$$\mathcal{L}_{\mathbf{u},\boldsymbol{\Phi}}\boldsymbol{\tau} = \frac{\partial\boldsymbol{\tau}}{\partial t} + \mathbf{u}\nabla\boldsymbol{\tau} - \boldsymbol{\Phi}\boldsymbol{\tau} - \boldsymbol{\tau}\boldsymbol{\Phi}^T, \tag{2.32}$$

where again the Eulerian form of the total derivative has been used. The parameter a is known as the slippage parameter. The slippage parameter is related to how much energy is transmitted to the bulk fluid as viscoelastic particles slide through the bulk.

In [30, 31] it is shown that the form of the equations (2.30), (2.31) and (2.32) is that of a SMRDE,

$$\frac{D\boldsymbol{\zeta}(t)}{Dt} = A\boldsymbol{\zeta} + \boldsymbol{\zeta}A^T - \boldsymbol{\zeta}B\boldsymbol{\zeta}^T + G. \tag{2.33}$$

A general SMRDE can be rewritten using a Lie derivative $\mathcal{L}_{\mathbf{u},\boldsymbol{\Phi}}\boldsymbol{\zeta} = G$, by setting $\boldsymbol{\Phi} = A - \frac{1}{2}B\boldsymbol{\zeta}$ and taking advantage of properties of symmetric second order tensors. The solution to the SMRDE can be developed and requires a transition matrix $\mathbf{L}$ that satisfies (2.21).

Now that it has been shown how a SMRDE can be written as a Lie derivative and that the Truesdell stress rate, (2.26), is a Lie derivative, these relationships are used to solve the stress PDE, (2.6). However, before the solution to (2.6) is discussed, the Oldroyd-B stress model is shown to be equivalent to (2.6). The modified Oldroyd-B stress model used in this work is,

$$\boldsymbol{\tau} + \mathrm{Wi}\varphi\left(\frac{\partial\boldsymbol{\tau}(t)}{\partial t} + \mathbf{u}\nabla\boldsymbol{\tau}(t) - \nabla\mathbf{u}(t)\,\boldsymbol{\tau}(t) - \boldsymbol{\tau}(t)\,\nabla\mathbf{u}(t)^T\right) = 2\eta_p\varphi D(\mathbf{u}), \tag{2.34}$$

where $\mathrm{Wi} = \lambda U_0 L_0 = \lambda/T_0$ is the Weissenberg number. In the modification of the Oldroyd-B model introduced in this work is the multiplication, of Wi, by the biofilm volume fraction, φ. Note, Wi is dependent on the relaxation time, λ, and the time scale T_0. By changing the relaxation time or the characteristic time, a problem can

change from a high Weissenberg number problem (Wi >> 1) to a low Weissenberg number problem (Wi << 1).

When the Weissenberg number is large, numeric methods predict large, erroneous stresses when describing viscoelastic fluid flowing through physical contractions [15]. In this work a viscous fluid does exhibit contracting flow, as it flows over and around a polymer, however, the viscoelastic fluid does not flow through a contraction. Therefore, the HWNP is not an issue in this work at this time. Dupret [14], showed that the symmetry of the numeric form of the stress tensor must be preserved this symmetry is critical for maintaining the stability of the numeric method in the sense of Hadamard. Next the Oldroyd-B model is shown to be a Lie derivative and by extension a SMRDE. The purpose is to demonstrate that all the developments concerning the Lie derivative apply to the classic Oldroyd-B stress model.

In order to show that the Oldroyd-B model can be written as a Lie derivative first consider $\mathcal{L}_{\mathbf{u},\nabla\mathbf{u}}\left(\boldsymbol{\tau}+\frac{\eta_p}{\mathrm{Wi}}\boldsymbol{I}\right)$. Since the Lie derivative is a linear operator the effects of applying the Lie derivative to each term is considered separately. This particular Lie derivative acting upon $\boldsymbol{\tau}$ gives the UCD,

$$\mathcal{L}_{\mathbf{u},\nabla\mathbf{u}}\left(\boldsymbol{\tau}\right)=\frac{\partial\boldsymbol{\tau}\left(t\right)}{\partial t}+\mathbf{u}\nabla\boldsymbol{\tau}\left(t\right)-\nabla\mathbf{u}\left(t\right)\boldsymbol{\tau}\left(t\right)-\boldsymbol{\tau}\left(t\right)\nabla\mathbf{u}\left(t\right)^{T}, \tag{2.35}$$

which is (2.30) with the total derivative (2.25) written out. The reader should note that this expression is a substantial component of the Oldroyd-B model, (2.34). The application of the Lie derivative to the identity tensor, $\boldsymbol{I}$, gives the well known symmetric part of the velocity field since the total derivative of a constant is the zero tensor. This is,

$$\mathcal{L}_{\mathbf{u},\nabla\mathbf{u}}\boldsymbol{I}=-2D(\mathbf{u}). \tag{2.36}$$

Then the Oldroyd-B model (2.34) can be written as, $\boldsymbol{\tau} + \mathrm{Wi}\varphi\mathcal{L}_{\mathbf{u},\nabla\mathbf{u}}\boldsymbol{\tau} = -\eta_p\varphi\mathcal{L}_{\mathbf{u},\nabla\mathbf{u}}\boldsymbol{I}$ and use the linearity of the Lie derivative operator to get,

$$\boldsymbol{\tau} + \mathrm{Wi}\varphi\mathcal{L}_{\mathbf{u},\nabla\mathbf{u}}\left(\boldsymbol{\tau} + \frac{\eta_p}{\mathrm{Wi}}\boldsymbol{I}\right) = \mathbf{0}. \tag{2.37}$$

Now add $\frac{\eta_p}{\mathrm{Wi}}\mathbf{I}$ to both sides of (2.37),

$$\boldsymbol{\tau} + \frac{\eta_p}{\mathrm{Wi}}\mathbf{I} + \mathrm{Wi}\varphi\mathcal{L}_{\mathbf{u},\nabla\mathbf{u}}\left(\boldsymbol{\tau} + \frac{\eta_p}{\mathrm{Wi}}\boldsymbol{I}\right) = \frac{\eta_p}{\mathrm{Wi}}\mathbf{I}. \tag{2.38}$$

Then make the substitution of the so-called conformation stress, $\mathbf{c}$, defined here,

$$\mathbf{c} = \boldsymbol{\tau} + \frac{\eta_p}{\mathrm{Wi}}\mathbf{I}. \tag{2.39}$$

Then

$$\varphi\mathcal{L}_{\mathbf{u},\nabla\mathbf{u}}(\mathbf{c}) + \alpha\mathbf{c} = \beta\mathbf{I}, \tag{2.40}$$

where $\alpha = \frac{1}{\mathrm{Wi}}$ and $\beta = \frac{\eta_p}{\mathrm{Wi}^2}$. The subtle change from the stress model presented in [30, 31] and the stress model, (2.6), finally must be addressed. The scaling by the polymer volume fraction, φ, in (2.6), means that the solution proposed in [30,31] cannot be used without first making an argument. The argument proceeds as follows, for non-zero values of the polymer volume fraction, φ, divide both sides of the stress partial differential equation by the polymer volume fraction, φ, incorporate, φ, into the α and β expressions and use the solution described in [30, 31]. However, below some small threshold value of the polymer volume fraction, φ, the elastic stress is essentially zero, the stress partial differential equation does not need to be solved and the contribution to the Navier-Stokes equation from the elastic stress is essentially zero. In this way the division by zero can be avoided because no solution is attempted.

Note that the Oldroyd-B model can be rewritten in the form of a SMRDE, (2.33), using $A = \frac{1}{2\mathrm{Wi}}\mathbf{I} - \nabla\mathbf{u}$, $B = 0$ and $G = \frac{\eta_p}{\mathrm{Wi}}\mathbf{I}$. Then immediately, the transition matrix satisfies (2.21) and the process developed above can be used to solve for the transition matrix, which in the Oldroyd-B model case, is the conformation stress, $\mathbf{c}$. Note that if instead the parameter β is defined as $\beta = \frac{\eta_p}{a\mathrm{Wi}^2}$, then the Johnson-Segalman objective rate has been used which translates into the Gordon-Schowalter derivative. Once again, this can be found in [30, 31].

Advection Equation:

The next DE is the advection equation, (2.7). The biofilm volume fraction has been assigned the variable, φ. Growth is not considered because the time scale for the model is orders of magnitude less than a growth time scale. The advection equation states that the material derivative of the biofilm volume fraction, over the velocity field $\mathbf{u}$ is zero.

Eulerian Lagrangian Method:

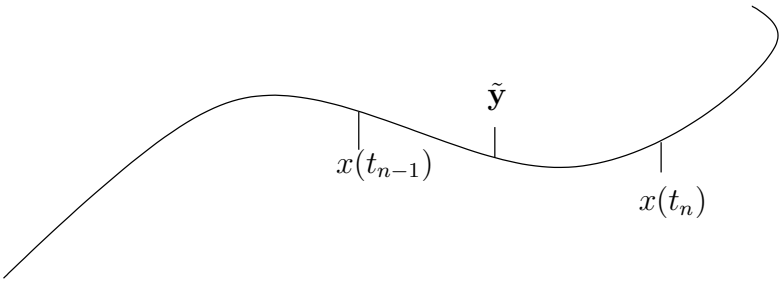
The NSE (2.3) is solved using the Eulerian Lagrangian method (ELM). The ELM uses a forward Euler approximation of the time derivative in the NSE. The previous locations of viscoelastic particles are a function of the velocity field. These points in the past are referred to collectively as departure feet and individually as a departure foot. The departure feet DE is derived from equation (2.11) by setting $s = t$ and so the departure feet DE is implicitly defined by,

$$\frac{\partial \mathbf{x}}{\partial t} = \mathbf{u}\left(\frac{\tilde{\mathbf{y}} + \mathbf{x}}{2}, t\right), \tag{2.41}$$

where $\tilde{\mathbf{y}}$ is the departure foot. It should be noted that (2.41) is a restated version of (2.11).

While the departure foot DE is not an explicit component of the system of equations that models viscoelastic fluid flow, it is fundamental to the solution of that system. So, the departure foot DE is discussed here. Since derivatives with respect to time need to be numerically approximated in the Navier-Stokes equation (2.3) and the stress PDE (2.6), there is a need to determine where parcels of fluid were physically located in the past, as in Figure 2.2, before they arrived at a node or Gaussian quadrature point in the present. In the figure the perfect departure foot, $\tilde{\mathbf{y}}$, on the streamline, is depicted between the current $\mathbf{x}(t_n)$ and the past $\mathbf{x}(t_{n-1})$ positions. These positions from the past are called Departure Feet in honor of the work in [30,31] wherein this naming convention is used. The reason that these positions need to be known is because the elastic stress at these past locations effects the elastic stress at the current location. The implicit solution to (2.41), determined using Newton's method is discussed in the numeric model section.

Figure 2.2: A flow line depicting a departure foot.



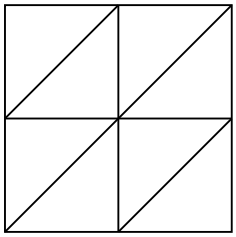
The solution to the departure foot DE (2.41) has a CFL type condition, the violation of which causes the method to become unstable. The instability is attributed to the lack of continuity of the gradient of the velocity. Since the solution to the departure foot algorithm depends upon the gradient of the velocity this continuity

issue is disastrous should a departure foot be required to leave the element it initially occupied. The original element requirement for the departure feet is likely the result of the FEM solution to the velocity. The FEM velocity solution in produces a surface that is continuous but where the gradient is discontinuous. This gradient continuity issue can be addressed by increasing the number of degrees of freedom for each element. This has not been done in this work. So, if the product of the time step and the magnitude of the velocity, at a point, is too large then a departure foot will leave its original element. Hence, the limitation to the size of this product which is not unlike a CFL condition. This is the only incidence of instability that the numeric solution to the model has ever exhibited.

Finite Element Model:

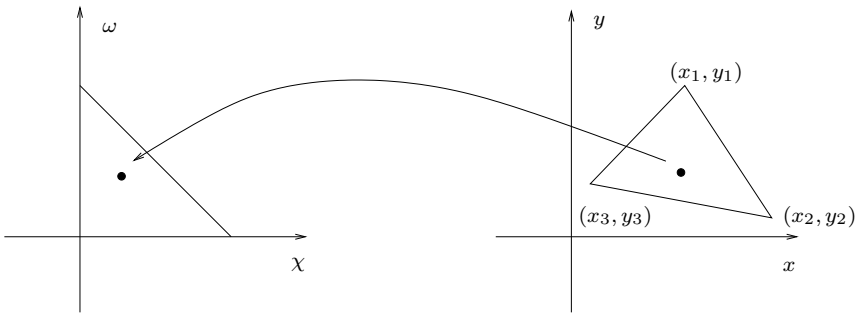
The finite element method developed in [47] is used to compute the solutions to the system of PDEs introduced in this work. The finite element method begins with the weak form of the Eulerian Lagrangian method (ELM). The domain is partitioned using, in this case, triangles. Figure 2.3 shows a 4X4 triangle partitioning. A discrete mesh of points, based on the degree of basis functions used, is then placed on this grid of elements. Using piece-wise defined polynomials, quadratic and linear in this work, as basis functions that are then defined on the points of each element. The velocity and pressure are approximated as linear combinations of these basis functions where the scaling coefficients are unknown. After substitution of the approximations into weak forms a system of algebraic equations is obtained. These integral equations are approximated using Gaussian quadrature, 13 point in each element and 4 point on the boundary of the domain. The barycentric coordinates and weights for these points are listed in Tables 2.3 and 2.4.

Figure 2.3: A 4X4 triangle partitioning of the domain.



The degree of the basis functions used to approximate the various physical properties in the presented model are quadratic basis functions for the biofilm volume fraction, the three stress tensor components and the horizontal and vertical velocities. Linear basis functions are used for the pressure. In order to satisfy the so called inf-sup condition [16] the degree of the basis functions used for the pressure must be less than the degree used for the velocity basis functions. The classic Taylor-Hood element, which satisfies the inf-sup condition, is used in this work and presented in [53]. For a 2-D triangular mesh there are three linear basis functions and six quadratic basis functions. These basis functions are described in terms of the so called barycentric coordinates, χ, ω. Each of the triangular elements can be transformed into a single reference triangle in barycentric coordinates, see Figure 2.4. The following are a list of the linear and quadratic basis functions in barycentric coordinates that have been used.

Figure 2.4: Transform a coordinate using a reference triangle.



Linear Basis Functions:

$$LBf_1 = \chi, \quad LBf_2 = \omega, \quad LBf_3 = 1 - \chi - \omega. \tag{2.42}$$

Quadratic Basis Functions:

$$\begin{aligned} &QBf_1 = \chi(2\chi - 1), && QBf_2 = 4\chi\omega, \\ &QBf_3 = \omega(2\omega - 1), && QBf_4 = 4\omega(1 - \chi - \omega), \\ &QBf_5 = (1 - \chi - \omega)(2(1 - \chi - \omega) - 1), && QBf_6 = 4\chi(1 - \chi - \omega). \end{aligned} \tag{2.43}$$

Partials of the Linear Basis Functions:

$$\begin{aligned} &\frac{\partial LBf_1}{\partial \chi} = 1, && \frac{\partial LBf_1}{\partial \omega} = 0, \\ &\frac{\partial LBf_2}{\partial \chi} = 0, && \frac{\partial LBf_2}{\partial \omega} = 1, \\ &\frac{\partial LBf_3}{\partial \chi} = -1, && \frac{\partial LBf_3}{\partial \omega} = -1. \end{aligned} \tag{2.44}$$

Partials of the Quadratic Basis Functions:

$$\begin{aligned} &\frac{\partial QBf_1}{\partial \chi} = 4\chi - 1, && \frac{\partial QBf_1}{\partial \omega} = 0, \\ &\frac{\partial QBf_2}{\partial \chi} = 4\omega, && \frac{\partial QBf_2}{\partial \omega} = 4\chi, \\ &\frac{\partial QBf_3}{\partial \chi} = 0 && , \frac{\partial QBf_3}{\partial \omega} = 4\omega - 1, \\ &\frac{\partial QBf_4}{\partial \chi} = -4\omega, && \frac{\partial QBf_4}{\partial \omega} = 4(1 - \chi - 2\omega), \\ &\frac{\partial QBf_5}{\partial \chi} = -4(1 - \chi - \omega) + 1, && \frac{\partial QBf_5}{\partial \omega} = -4(1 - \chi - \omega) + 1, \\ &\frac{\partial QBf_6}{\partial \chi} = 4(1 - 2\chi - \omega), && \frac{\partial QBf_6}{\partial \omega} = -4\chi. \end{aligned} \tag{2.45}$$

The coordinates of Gaussian quadrature points, see Tables 2.3, 2.4, for every triangular element, need to be converted from barycentric to Cartesian coordinates, in order to determine their departure feet and then converted back to barycentric for use in the basis functions. The departure feet for the Gaussian quadrature points when solving (2.3) for the velocity and pressure are needed. The departure feet for all of the quadratic nodes for each element need to be converted into barycentric coordinates when solving (2.6) locally for the stress tensor components. The vertices of a triangular element are used to determine the barycentric coordinates of a Gaussian quadrature point. Given Cartesian coordinates, $(x_1, y_1), (x_2, y_2)$ and (x_3, y_3) for the vertices of an element and a Cartesian point (x_0, y_0) whose corresponding barycentric point is given by the following sequence of calculations. The barycentric coordinates; (χ_0, ω_0), are given by,

$$\begin{aligned} \chi_0 &= \frac{1}{2A}((x_0 - x_3)(y_2 - y_3) - (y_0 - y_3)(x_2 - x_3)), \\ \omega_0 &= \frac{1}{2A}((x_0 - x_1)(y_3 - y_1) - (y_0 - y_1)(x_1 - x_3)), \end{aligned} \tag{2.46}$$

where

$$\begin{aligned} \alpha_1 &= x_2 y_3 - x_3 y_2, \\ \alpha_2 &= x_3 y_1 - x_1 y_3, \\ \alpha_3 &= x_1 y_2 - x_2 y_1, \\ A &= \tfrac{1}{2}(\alpha_1 + \alpha_2 + \alpha_3). \end{aligned} \tag{2.47}$$

The cartesian coordinates, (x_0, y_0), are given by,

$$x_0 = \frac{1}{b_1 c_2 - c_1 b_2}(c_2 a_1 - c_1 a_2),$$
$$y_0 = \frac{1}{b_1 c_2 - c_1 b_2}(b_1 a_2 - b_2 a_1), \tag{2.48}$$

where

$$a_1 = 2A\chi_0 + x_3(y_2 - y_3) - y_3(x_2 - x_3),$$
$$b_1 = y_2 - y_3,$$
$$c_1 = x_3 - x_2,$$
$$a_2 = 2A\omega_0 + x_1(y_3 - y_1) + y_1(x_1 - x_3),$$
$$b_2 = y_3 - y_1,$$
$$c_2 = x_1 - x_3. \tag{2.49}$$

13 Pt 2-D Gaussian Quadrature		
χ	ω	Weight
$\frac{1}{3}$	$\frac{1}{3}$	-0.149570044467670
0.479308067841923	0.260345966079038	0.175615257433204
0.260345966079038	0.479308067841923	0.175615257433204
0.260345966079038	0.260345966079038	0.175615257433204
0.869739794195568	0.065130102902216	0.053347235608839
0.065130102902216	0.869739794195568	0.053347235608839
0.065130102902216	0.065130102902216	0.053347235608839
0.638444188569809	0.312865496004875	0.077113760890257
0.312865496004875	0.638444188569809	0.077113760890257
0.638444188569809	0.048690315425316	0.077113760890257
0.048690315425316	0.638444188569809	0.077113760890257
0.048690315425316	0.312865496004875	0.077113760890257
0.312865496004875	0.048690315425316	0.077113760890257

Table 2.3: 13 Point 2-D Gaussian Quadrature

4 Pt 1-D Gaussian Quadrature	
χ	Weight
0	0.65214515
0.33998194	0.65214515
-0.33998194	0.34785485
-0.86113631	0.34785485

Table 2.4: 4 Point 1-D Gaussian Quadrature

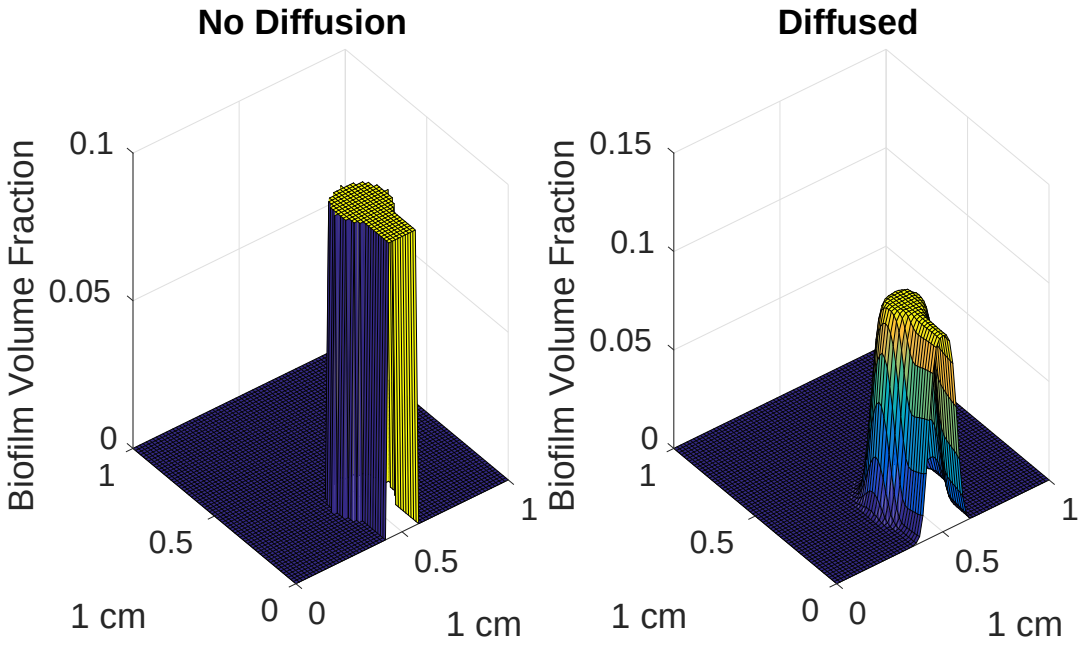
Initial Conditions:

The initial conditions are quite simple. Initially, the velocity, the pressure and the stress, are set equal to zero. However, the biofilm volume fraction is initialized with a value of 0.1 for various initial profiles. These different cases are detailed in Chapter 4. The initial configuration of the polymer is "softened" by diffusion so that the transition region from polymer to solvent is differentiable, i.e., there are no corners. This "softening" diffusion is implemented using only diffusion with no advection and is described by (2.50) next,

$$\frac{\partial \varphi}{\partial t} = \nabla \cdot (D_{\text{coeff}} \nabla \varphi) \,. \tag{2.50}$$

The diffusion softening effects applied to an initial biofilm profile that has a stalk and bulb in the middle of the domain is graphed in Figure 2.5. The rounded edges of the "softened" initial biofilm profile ensure that the spatial derivatives exist across these sharp transitions. The diffusion process is run for 8000 iterations in order to eliminate the oscillations that persist for thousands of iterations on the boundary of the biofilm. The diffusion coefficient for this softening is very small so that over the course of the thousands of iterations the biofilm does not substantially diffuse away. It should be noted that the softening diffusion coefficient is at least an order of

Figure 2.5: Effects of initial diffusion on bulb biofilm in the middle of the domain.

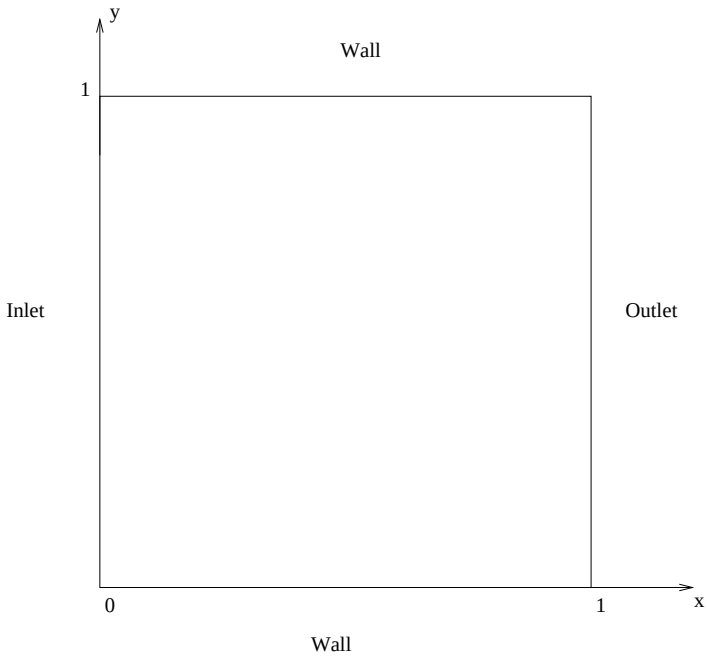


magnitude greater than the diffusion that is artificially introduced into the advection equation in order to stabilize the numerics. The number of time steps that are used in the results section are more than an order of magnitude less than the 8000 used here. Hence, the impacts of the artificial diffusion introduced into the advection equation are negligible. This is discussed in more detail in Chapter 3.

Boundary Conditions:

The boundary conditions for the velocity are what one would expect, no slip at the walls, prescribed inlet and equilibrium at the exit. The velocity has Dirichlet boundary conditions on the top, bottom and front of the domain. The boundary conditions at the exit are mixed; Dirichlet for the the vertical velocity and Neumann for the horizontal velocity. On the top, $y = 1$, and bottom ,$y = 0$, of the domain

Figure 2.6: Domain and boundaries.



(2.11)

both the vertical and horizontal velocities are set constant and equal to zero. At the inlet, $x = 0$, of the domain the vertical velocity is constant and zero. However, the horizontal velocity at the inlet of the domain is more complicated. Initially, at $t = 0$, the inlet horizontal velocity is zero. For non-zero time the inlet boundary condition is a quadratic that grows over a specific amount of time until reaching a predetermined maximum. Beginning with the quadratic profile, $4y(1-y)$, and scaling by an increasing function that grows to a prescribed maximum of 0.1. The maximum of the initial quadratic is one and occurs at $y = 0.5$. This maximum was chosen by trial and error so that the apparent CFL condition on the hidden departure foot algorithm could be met with a larger time step value of $0.1\triangle x$. The inlet horizontal boundary condition is scaled by an increasing function that ramps up slowly over time. This ramp function provides a method by which the inflow can be increased. The ramp function is as follows,

$$\text{ramp} = 0.1\sin(\text{F}t), \tag{2.51}$$

where $\text{F} = \frac{\pi}{2\text{RampTime}}$ and RampTime is $50\triangle t$. The ramp time is the length of time assigned for the quadratic inlet horizontal velocity boundary condition function maximum to increase from zero to 0.1. The size of the ramp time was chosen to be 50 time steps, i.e., $50\triangle t$, so as to smooth out the changes to the system and there by avoid "shocking" the velocity profile. The complete inlet horizontal boundary condition function for $0 \leq t \leq \text{RampTime}$ is,

$$\mathbf{u}(x,y,t)\Big|_{x=0} = \mathbf{u}(0,y,t) = \sin(\text{F}t)0.4y(1-y), \tag{2.52}$$

and for $\text{RampTime} < t$, $\mathbf{u}(0,y,t) = 0.4y(1-y)$. This inlet horizontal boundary condition is used until a prescribed time is attained. The inlet boundary condition is then ramped down using the same process but with the cosine function instead of sine.

The boundary conditions on the exit are as the follows.

$$\begin{aligned} \nabla u(x,y,t)|_{x=1} &= 0, \\ v(1,y,t) &= 0, \\ \varphi(0,y,t) &= 0, \\ \nabla\varphi(x,y,t)|_{x=1} &= 0, \\ \nabla\varphi(x,y,t)|_{y=0} &= 0, \\ \nabla\varphi(x,y,t)|_{y=1} &= 0. \end{aligned} \tag{2.53}$$

The exit vertical velocity, v, has Dirichlet BCs set equal to zero and the horizontal velocity, u has Neumann BCs set equal to zero. The biofilm volume fraction, φ, has zero Dirichlet BC at the inlet and zero Neumann BCs on the top and bottom. The BC for the biofilm volume fraction at the exit is Neumann set equal to zero. This could be an issue if the polymer were ever to run into the exit boundary. For this work the amount of real world time necessary for this to occur is computationally prohibitive. The pressure and stress do not have any BCs. In fact, assigning even a single pressure boundary condition, over determines the system.

NUMERICAL METHODS

The numerical methods chapter begins with the algorithm produces the solutions presented in Chapter 4. Then what follows is a development of the mathematic equations for the numeric methods used to solve for the departure feet, the horizontal and vertical velocities, pressure, stress and biofilm volume fraction. The resulting system of linear equations is solved using parallel processing with the Trilinos library called AztecOO.

Numeric Model:

The numeric methods developed in this chapter are developed in a specific order, originally developed in [30,31] and then modified here in this work. The change to the algorithm from [30,31] is the addition of an advection equation applied to the biofilm volume fraction. Since the heart of the numeric solution to the system of DEs which describe the viscoelastic behavior of biofilm flow is this algorithm, the algorithm is described prior to the introduction of of the numeric methods.

Algorithm:

There are several numeric methods that must be discussed. The numerics for the coupled system of the departure feet, pressure, velocities, stresses and biofilm DEs are detailed shortly. The order in which these DEs are solved is enumerated below. An outline of the algorithm starts at time step t_n. The departure feet for all Gaussian quadrature points, shown in Tables 2.3, 2.4 and quadratic nodes are first determined. Then velocity, pressure and stress are solved iteratively. Using the iteration index l the terms associated with this index at time step n for the velocity,

pressure and stress are $\mathbf{u}^{n,l}$, $p^{n,l}$ and $\boldsymbol{\tau}^{n,l}$ respectively. First, assume that the velocity, pressure and stress are known for iteration step l. Now solve for the velocity and pressure at iteration step $l+1$ using the Trilinos iterative (yes yet another level of iteration) solver built into the AztecOO library using a sparse matrix and parallel processing. Next the velocity at iteration step $l+1$, which is $\mathbf{u}^{n,l+1}$, is used to solve for the next iteration of the stress $\boldsymbol{\tau}^{n,l+1}$. It should be noted the departure feet are not recomputed for each l iteration. The new velocities, pressures and stresses all depend on these departure feet. This l iteration process is repeated until the exit condition $\|\mathbf{u}^{n,l+1}-\mathbf{u}^{n,l}\|_{L2}+\|p^{n,l+1}-p^{n,l}\|_{L2} < \text{Tol}$, where Tol is some tolerance, is met. Once the exit condition is met then it is assumed that the velocity and pressure have converged, the time step is iterated and the velocity, pressure and stress assignments are made,

$$\mathbf{u}^{n,l+1} = \mathbf{u}^{n+1,0}, p^{n,l+1} \qquad = p^{n+1,0}, \boldsymbol{\tau}^{n,l+1} = \boldsymbol{\tau}^{n+1,0}. \tag{3.1}$$

Finally, $\mathbf{u}^{n+1,0}$ is used to solve for the biofilm volume fraction in the advection equation for the biofilm volume fraction at time step $n+1$ is, ϕ^{n+1}. This process is repeated for the time iteration index n until the number of time steps needed to create a simulation is completed.

1. Solve Departure Foot at time t_n: $\tilde{\mathbf{y}}^n$
2. Iteratively Solve Navier-Stokes for time t_{n+1}: $\mathbf{u}^{n,l}$, $p^{n,l}$
3. Locally Solve Stress for time t_{n+1}: $\boldsymbol{\tau}^{n,l}$
4. Solve Advection for time t_{n+1}: ϕ^{n+1}

The numeric methods for each of these DEs are developed in order; softening diffusion, departure feet, Navier-Stokes, Stress and finally the advection equation.

Softening Diffusion:

In Chapter 2 the diffusion based "softening" of the initial biofilm volume fraction surface was introduced. Below, (3.2), (3.3), are the discrete weak forms for the diffusion equation, (2.50). The global matrix entries are,

$$[\mathbf{A}]_{i,j} = \int_e \phi_i \phi_j + \varphi^{\text{old}} D_{\text{coeff}} k \left(\frac{\partial \phi_i}{\partial x} \frac{\partial \phi_j}{\partial x} + \frac{\partial \phi_i}{\partial y} \frac{\partial \phi_j}{\partial y} \right) \text{dA}, \tag{3.2}$$

where $[\mathbf{A}]_{i,j}$ is the (i,j) element of the matrix $\mathbf{A}$, k is the time step $\triangle t$, ϕ_i are the quadratic test functions and φ^{old} is the known biofilm volume fraction. The right hand side (RHS) entries are,

$$[\mathbf{F}]_i = \int_e \varphi^{\text{old}} \phi_i \text{dA}, \tag{3.3}$$

where $[\mathbf{F}]_i$ is the ith component of the right hand side vector. This diffusion is run for 8000 time steps with a small diffusion coefficient of 10^{-5} and relatively large time step $\triangle t = 1.0 \triangle x$. The global matrix $\mathbf{A}$ is size $N_{\text{quad}} \times N_{\text{quad}}$, where N_{quad} is the number of quadratic nodes in the mesh. The RHS vector $\mathbf{F}$ has length N_{quad}. The numeric solution to the departure feet DE is discussed next.

Departure Feet:

The algorithm begins with solving for the departure feet for the Gaussian quadrature points and the quadratic nodes of the mesh over the velocity field, $\mathbf{u}$. So, the departure feet numeric method is introduced first. As a reminder, the departure feet are necessary because the ELM requires that the horizontal and veritcal velocities as well as the elastic stress of the fluid at time step t_n are known in the past t_{n-1}.

This previous velocities and elastic stresses are found by following a characteristic backwards in time. These characteristic trajectories are functions of the gradient of the velocity field $\nabla \mathbf{u}$. The numerics that capture these departure feet are introduced next.

While it is possible to solve for the departure feet explicitly such a scheme doesn't preserve volume [30,31]. So, the departure feet DE must be solved implicitly. First an approximate solution for the departure feet is assigned the variable, $\tilde{\mathbf{y}}$. A departure foot $\tilde{\mathbf{y}}$ is where a point $(\mathbf{x}, t)$ was at time $(t - \triangle t)$. There are more complex volume preserving schemes available but they have not been investigated. Applying the simplest implicit volume preserving scheme to (2.41) gives,

$$\frac{\mathbf{x} - \tilde{\mathbf{y}}}{k} = \mathbf{u}(\frac{\tilde{\mathbf{y}} + \mathbf{x}}{2}, t), \tag{3.4}$$

where again, $k = \triangle t$, is the time step size. The implicit equation for the departure feet is then,

$$\tilde{\mathbf{y}} = x - k\mathbf{u}(\frac{\tilde{\mathbf{y}} + \mathbf{x}}{2}, t). \tag{3.5}$$

The function $\mathbf{G}(\mathbf{y})$, is defined

$$\mathbf{G}(\mathbf{y}) = \mathbf{y} - \mathbf{x} + k\mathbf{u}(\frac{\mathbf{y} + \mathbf{x}}{2}, t), \tag{3.6}$$

where $\mathbf{x}$ and t are constants. Then $\tilde{\mathbf{y}}$ is the approximate solution to $\mathbf{G}(\mathbf{y}) = \mathbf{0}$. The Newton's method solution begins with the linearization of $\mathbf{G}$,

$$\mathbf{L}(\mathbf{y}) = \nabla \mathbf{G}(\mathbf{y}_0)(\mathbf{y} - \mathbf{y}_0) + \mathbf{G}(\mathbf{y}_0), \tag{3.7}$$

where $\mathbf{y}_0$ is the initial guess. The Cartesian coordinate of a Gaussian quadrature point or quadratic mesh node are used as the initial guess. Then, per the standard Newton's method used to solve nonlinear equations, a sequence $\mathbf{y}_n$ is introduced. It is assumed that if the sequence converges it converges to $\tilde{\mathbf{y}}$. The terms of the sequence are defined iteratively by,

$$\mathbf{y}_{n+1} = \mathbf{y}_n - (\nabla \mathbf{G}(\mathbf{y}_n))^{-1}\mathbf{G}(\mathbf{y}_n), \tag{3.8}$$

where $\nabla \mathbf{G}(\mathbf{y}_n) = \mathbf{I} + \frac{k}{2}\nabla \mathbf{u}(\frac{\mathbf{y}_n+\mathbf{x}}{2}, t)$ and where $\mathbf{y}_0$ and $\mathbf{x}$ are both either Gaussian quadrature points or quadratic nodes and $\mathbf{y}_n \to \tilde{\mathbf{y}}$ as $n \to \infty$. The gradient of the velocity is at the heart of the solution for the departure feet. This is the likely cause of errors should the location of a departure foot ever be found outside of the element in which the original point resided. By definition, the 2D velocity is.

$$\mathbf{u} = \begin{bmatrix} u(x,y) \\ v(x,y) \end{bmatrix}, \tag{3.9}$$

and the gradient of the velocity is,

$$\nabla \mathbf{u} = \begin{bmatrix} u_x & u_y \\ v_x & v_y \end{bmatrix}. \tag{3.10}$$

By letting $\det(\nabla \mathbf{u})$ and $\mathrm{tr}(\nabla \mathbf{u})$ denote the determinant and trace of $\nabla \mathbf{u}$ respectively. Then it can be shown that

$$(\nabla \mathbf{G})^{-1} = \frac{1}{1 + \frac{k}{2}\mathrm{tr}(\nabla \mathbf{u}) + \frac{k^2}{4}\det(\nabla \mathbf{u})} \left(\mathbf{I} + \tfrac{k}{2}\det(\nabla \mathbf{u})(\nabla \mathbf{u})^{-1}\right). \tag{3.11}$$

The form of equation (3.11) will be seen again in the numerics section when determining the numeric solution to the stress PDE.

The finite element approximations for $\mathbf{u}$ and $\nabla\mathbf{u}$ are used when solving for $\tilde{\mathbf{y}}$. Once again, a hidden CFL type condition has been discovered for large values of $\|\mathbf{u}(\mathbf{x}(t),t)\|\triangle t$, where $\|\mathbf{u}(\mathbf{x}(t),t)\|$ is the magnitude of the velocity at position $\mathbf{x}(t)$ and time t. The violation of this CFL condition causes a break down in convergence and eventual failure of this numeric method. This CFL condition is likely the result of the finite element method producing solutions that are only C^0 and not C^1. Since the gradient of the velocity is a discontinuous surface and the departure feet solution depends on the continuity of the gradient of the velocity, this is likely the cause of the observed instability. A horizontal velocity surface with oscillations caused by this instability is presented and discussed in Chapter 4. The NSE, (2.3), solution is discussed next.

Finite Element:

The finite element method used to approximate the solutions to the velocity and pressure is now presented. The velocity is approximated using quadratic elements and the pressure is, for stability concerns, approximated on linear elements [53]. Numeric integration is performed on each element using 2-D thirteen point Gaussian quadrature and four point 1-D Gaussian quadrature on the boundary. The FEM approximation on element e for the horizontal and vertical velocity is

$$\mathbf{u}_e(x,y) = \begin{bmatrix} u_{1,e}(x,y) \\ u_{2,e}(x,y) \end{bmatrix} = \begin{bmatrix} \sum_{i=1}^{6} u_{1,i}\phi_i(x,y) \\ \sum_{i=1}^{6} u_{2,i}\phi_i(x,y) \end{bmatrix}, \tag{3.12}$$

where the $\phi_i(x,y)$ are the quadratic basis functions described in (2.43) and $u_{1,i}$ and $u_{2,i}$ are the values of horizontal and vertical velocity at the quadratic element nodes.

The FEM approximation on element e for the pressure are

$$p_e(x,y) = \sum_{k=1}^{3} p_i \psi_i(x,y), \tag{3.13}$$

where the $\psi_i(x,y)$ are the linear basis functions described in (2.42) and p_i are the values of the pressure at the linear element nodes.

The velocity test function vectors are

$$\mathbf{v}_e^{1,j}(x,y) = \begin{bmatrix} \phi_j(x,y) \\ 0 \end{bmatrix}, \mathbf{v}_e^{2,j}(x,y) = \begin{bmatrix} 0 \\ \phi_j(x,y) \end{bmatrix}, \tag{3.14}$$

and the pressure test functions are

$$q_e^j(x,y) = \psi_j(x,y). \tag{3.15}$$

Navier-Stokes:

The time derivative in the NSE, (2.3), is numerically approximated using forward Euler in accordance with the ELM. The reader should note the use of the departure foot notation in the equation below,

$$\begin{aligned} \mathrm{Re}_s \frac{\mathbf{u}}{k} = {} & 2\nabla \cdot \left[\left(1 + \varphi \left(\frac{\eta_p}{\eta_s} - 1 \right) \right) D(\mathbf{u}) \right] \\ & - \nabla p + \nabla \cdot \left(\varphi \left(\tilde{\mathbf{y}} \right) \boldsymbol{\tau} \left(\tilde{\mathbf{y}} \right) \right) + \mathrm{Re}_s \frac{\mathbf{u}\left(\tilde{\mathbf{y}} \right)}{k}. \end{aligned} \tag{3.16}$$

The notation from [30, 31] is reused in the weak forms that follow,

$$(\mathbf{a}, \mathbf{b}) = \int_e \mathbf{a} \cdot \mathbf{b} \mathrm{dA}, \tag{3.17}$$

where $\mathbf{a}$ and $\mathbf{b}$ are vectors and

$$(\mathbf{A} : \mathbf{B}) = \int_e \mathrm{tr}\left(\mathbf{AB}\right) \mathrm{dA}, \tag{3.18}$$

where $\mathbf{A}$ and $\mathbf{B}$ are tensors.

The weak form for equation (3.16) is,

$$\begin{aligned} &\left(\mathbf{v}_e, \mathrm{Re}_s \frac{\mathbf{u}_e^{\mathrm{new}}}{k}\right) + 2\left(1 + \varphi\left(\frac{\eta_p}{\eta_s} - 1\right)\right)\left(D\left(\mathbf{u}_e^{\mathrm{new}}\right) : D\left(\mathbf{v}_e\right)\right) \\ &- \left(\nabla \cdot \mathbf{v}_e, p_e^{\mathrm{new}}\right) = \left(\mathbf{v}_e, \mathrm{Re}_s \frac{\mathbf{u}_e^{\mathrm{old}}\left(\tilde{\mathbf{y}}\right)}{k}\right) - \left(\varphi\left(\tilde{\mathbf{y}}\right) \boldsymbol{\tau}_e^{\mathrm{new}}\left(\tilde{\mathbf{y}}\right) : D\left(\mathbf{v}_e\right)\right). \end{aligned} \tag{3.19}$$

There are two of these equations, one for the horizontal velocity and another for the vertical velocity, however at this stage the vertical velocity weak form is identical to the horizontal velocity weak form. The weak form for the incompressibility condition is,

$$\left(\nabla \cdot \mathbf{u}_e^{\mathrm{new}}, q_e\right) = 0. \tag{3.20}$$

The discrete versions of the weak forms follow. Starting with the horizontal velocity weak form,

$$\int_e \frac{\mathrm{Re}_s}{k}\phi_i \sum_{j=1}^{6} u_{1,j}\phi_j + 2\left(1+\varphi\left(\frac{\eta_p}{\eta_s}-1\right)\right)\frac{\partial\phi_i}{\partial x}\sum_{j=1}^{6} u_{1,j}\frac{\partial\phi_j}{\partial x}$$
$$+\left(1+\varphi\left(\frac{\eta_p}{\eta_s}-1\right)\right)\frac{\partial\phi_i}{\partial y}\sum_{j=1}^{6}\left(u_{1,j}\frac{\partial\phi_j}{\partial y}+u_{2,j}\frac{\partial\phi_j}{\partial x}\right)-\frac{\partial\phi_i}{\partial x}\sum_{k=1}^{3}p_k\psi_k\mathrm{dA}$$
$$=\int_e \frac{\mathrm{Re}_s}{k}\phi_i u_{1,e}^{\mathrm{old}}(\tilde{\mathbf{y}})-\left(\frac{\partial\phi_i}{\partial x}\tau_{1,1,e}^{\mathrm{old}}(\tilde{\mathbf{y}})+\frac{\partial\phi_i}{\partial y}\tau_{1,2,e}^{\mathrm{old}}(\tilde{\mathbf{y}})\right)\varphi(\tilde{\mathbf{y}})\mathrm{dA}. \tag{3.21}$$

Rewriting the weak form in order to pull out the variables $u_{1,i}$, $u_{2,i}$ and p_i from the integrals gives,

$$\sum_{j=1}^{6} u_{1,j}\int_e \frac{\mathrm{Re}_s}{k}\phi_i\phi_j+\left(1+\varphi\left(\frac{\eta_p}{\eta_s}-1\right)\right)\left(2\frac{\partial\phi_i}{\partial x}\frac{\partial\phi_j}{\partial x}+\frac{\partial\phi_i}{\partial y}\frac{\partial\phi_j}{\partial y}\right)\mathrm{dA}$$
$$+\sum_{j=1}^{6} u_{2,j}\int_e\left(1+\varphi\left(\frac{\eta_p}{\eta_s}-1\right)\right)\frac{\partial\phi_j}{\partial x}\frac{\partial\phi_i}{\partial y}\mathrm{dA}$$
$$-\sum_{k=1}^{3} p_k\int_e\frac{\partial\phi_i}{\partial x}\psi_k\mathrm{dA}$$
$$=\int_e\frac{\mathrm{Re}_s}{k}\phi_i u_{1,e}^{\mathrm{old}}(\tilde{\mathbf{y}})-\left(\frac{\partial\phi_i}{\partial x}\tau_{1,1,e}^{\mathrm{old}}(\tilde{\mathbf{y}})+\frac{\partial\phi_i}{\partial y}\tau_{1,2,e}^{\mathrm{old}}(\tilde{\mathbf{y}})\right)\varphi(\tilde{\mathbf{y}})\mathrm{dA}. \tag{3.22}$$

The discrete vertical velocity weak form is different from its horizontal counterpart and it is presented with the variables $u_{1,i}$, $u_{2,i}$ and p_i already factored out of the integrals,

$$\sum_{j=1}^{6} u_{1,j} \int_e \left(1+\varphi\left(\frac{\eta_p}{\eta_s}-1\right)\right) \frac{\partial\phi_j}{\partial y}\frac{\partial\phi_i}{\partial x}\mathrm{dA}$$
$$+\sum_{j=1}^{6} u_{2,j} \int_e \frac{\mathrm{Re}_s}{k}\phi_i\phi_j + \left(1+\varphi\left(\frac{\eta_p}{\eta_s}-1\right)\right)\left(2\frac{\partial\phi_i}{\partial x}\frac{\partial\phi_j}{\partial x}+\frac{\partial\phi_i}{\partial y}\frac{\partial\phi_j}{\partial y}\right)\mathrm{dA}$$
$$-\sum_{k=1}^{3} p_k \int_e \frac{\partial\phi_i}{\partial y}\psi_k \mathrm{dA}$$
$$=\int_e \frac{\mathrm{Re}_s}{k}\phi_i u_{1,e}^{\mathrm{old}}(\tilde{\mathbf{y}}) - \left(\frac{\partial\phi_i}{\partial x}\tau_{1,2,e}^{\mathrm{old}}(\tilde{\mathbf{y}})+\frac{\partial\phi_i}{\partial y}\tau_{2,2,e}^{\mathrm{old}}(\tilde{\mathbf{y}})\right)\varphi(\tilde{\mathbf{y}})\mathrm{dA}. \tag{3.23}$$

The weak form for the incompressibility equation is

$$0=\sum_{j=1}^{6} u_{1,j}\int_e \frac{\partial\phi_j}{\partial x}\psi_i \mathrm{dA} + \sum_{j=1}^{6} u_{2,j}\int_e \frac{\partial\phi_j}{\partial y}\psi_i \mathrm{dA} \tag{3.24}$$

The global matrix $\mathbf{A}$ is the assembly of 8 sparse matrices $\mathbf{A}_{11}$, $\mathbf{A}_{12}$, $\mathbf{A}_{21}$, $\mathbf{A}_{22}$, $\mathbf{B}_1$, $\mathbf{B}_2$, $\mathbf{B}_1^T$, $\mathbf{B}_2^T$ and a zero matrix, $\mathbf{0}$ and is shown next,

$$\mathbf{A}=\begin{bmatrix} \mathbf{A}_{11} & \mathbf{A}_{12} & \mathbf{B}_1 \\ \mathbf{A}_{21} & \mathbf{A}_{22} & \mathbf{B}_2 \\ \mathbf{B}_1^T & \mathbf{B}_2^T & \mathbf{0} \end{bmatrix}, \tag{3.25}$$

where the components of each matrix are given by the integral equations that follow shortly. The integrals are approximated using Gaussian quadrature. The whole system is

$$\mathbf{AU}=\mathbf{F}, \tag{3.26}$$

where $\mathbf{U}=[\mathbf{u},\mathbf{v},\mathbf{p}]^T$, $\mathbf{F}=[\mathbf{F}_1,\mathbf{F}_2,\mathbf{0}]^T$,

The matrix components for the global matrix (3.25) are,

$$[\mathbf{A}_{11}]_{i,j} = \int_e \frac{\mathrm{Re}_s}{k}\phi_i\phi_j + \left(1+\varphi\left(\frac{\eta_p}{\eta_s}-1\right)\right)\left(2\frac{\partial\phi_i}{\partial x}\frac{\partial\phi_j}{\partial x}+\frac{\partial\phi_i}{\partial y}\frac{\partial\phi_j}{\partial y}\right)\mathrm{dA}, \tag{3.27}$$

Due to the symmetry of the problem $[\mathbf{A}_{22}]_{i,j} = [\mathbf{A}_{11}]_{i,j}$. This is not true for the remaining matrices.

$$[\mathbf{A}_{12}]_{i,j} = \int_e \left(1+\varphi\left(\frac{\eta_p}{\eta_s}-1\right)\right)\frac{\partial\phi_j}{\partial x}\frac{\partial\phi_i}{\partial y}\mathrm{dA}, \tag{3.28}$$

$$[\mathbf{B}_1]_{i,k} = \int_e \frac{\partial\phi_i}{\partial x}\psi_k\mathrm{dA}, \tag{3.29}$$

$$[\mathbf{A}_{21}]_{i,j} = \int_e \left(1+\varphi\left(\frac{\eta_p}{\eta_s}-1\right)\right)\frac{\partial\phi_j}{\partial y}\frac{\partial\phi_i}{\partial x}\mathrm{dA}, \tag{3.30}$$

$$[\mathbf{B}_2]_{i,k} = \int_e \frac{\partial\phi_i}{\partial y}\psi_k\mathrm{dA}. \tag{3.31}$$

It should be noted that $\mathbf{A}_{12}^T = \mathbf{A}_{21}$ The right hand side vectors $\mathbf{F}_1$ and $\mathbf{F}_2$ are formed by the RHSs of (3.22) and (3.23) and have entries defined by the following,

$$[\mathbf{F}_1]_i = \int_e \frac{\mathrm{Re}_s}{k}\phi_i u_{1,e}^{\mathrm{old}}(\tilde{\mathbf{y}}) - \left(\frac{\partial\phi_i}{\partial x}\tau_{1,1,e}^{\mathrm{old}}(\tilde{\mathbf{y}})+\frac{\partial\phi_i}{\partial y}\tau_{1,2,e}^{\mathrm{old}}(\tilde{\mathbf{y}})\right)\varphi(\tilde{\mathbf{y}})\mathrm{dA}, \tag{3.32}$$

$$[\mathbf{F}_2]_i = \int_e \frac{\mathrm{Re}_s}{k}\phi_i u_{2,e}^{\mathrm{old}}(\tilde{\mathbf{y}}) - \left(\frac{\partial\phi_i}{\partial x}\tau_{1,2,e}^{\mathrm{old}}(\tilde{\mathbf{y}})+\frac{\partial\phi_i}{\partial y}\tau_{2,2,e}^{\mathrm{old}}(\tilde{\mathbf{y}})\right)\varphi(\tilde{\mathbf{y}})\mathrm{dA}. \tag{3.33}$$

The sizes of these matrices and vectors are determined by the number of nodes in the finite element mesh. The number of velocity nodes has been defined as N_{Quad} and, similarly, let the number of pressure nodes as N_{Lin}. The sizes of the $\mathbf{A}_{ij}$ matrices are N_{Quad} by N_{Quad} and the $\mathbf{B}$ matrices are N_{Quad} by N_{Lin}. The zero matrix is size N_{Lin} by N_{Lin}. The $\mathbf{F}$ vectors are of length N_{Quad} and there is a purely zero component to the right hand side vector of length N_{Lin}. The size of the global matrix $\mathbf{A}$ is $2N_{\text{Quad}}+N_{\text{Lin}}$ by $2N_{\text{Quad}}+N_{\text{Lin}}$.

Stress:

The numeric solution for the stress PDE begins with the discretization of the Lie derivative, (2.26), using backward Euler. First the notation substitution $\mathbf{L}(t;s,t) = \mathbf{E}(s,t), \mathbf{E}(s,s) = I$ is made out of respect for the notation choices in [30, 31]. It must be noted that the matrices which multiple the outside of the derivative in (2.26) become identity matrices when s is set equal to t. Hence, the numeric approximation of (2.26) is given by,

$$\begin{aligned}
&\frac{\partial\left(\mathbf{E}(s,t)\,\boldsymbol{\zeta}(s,t)\,\mathbf{E}(s,t)^T\right)}{\partial s}\bigg|_{s=t} \\
&\approx \frac{\mathbf{E}(s,t)\,\boldsymbol{\zeta}(s,t)\,\mathbf{E}(s,t)^T - \mathbf{E}(s-k,t)\,\boldsymbol{\zeta}(s-k,t)\,\mathbf{E}(s-k,t)^T}{k}\bigg|_{s=t}, \\
&= \frac{\boldsymbol{\zeta}(t,t) - \mathbf{E}(t-k,t)\,\boldsymbol{\zeta}(t-k,t)\,\mathbf{E}(t-k,t)^T}{k}
\end{aligned} \tag{3.34}$$

The connection between the Oldroyd-B stress constitutive equation, (2.34) and the Lie derivative, (2.26) has been established in Chapter 2. In order to numerically solve the Lie derivative, (2.26), a numeric solution for $\mathbf{E}(s,t)$ is required. Now,

returning to the transition matrix PDE which is restated here using $\mathbf{E}$ notation found in [31],

$$\frac{\partial \mathbf{E}(s,t)}{\partial t} = \mathbf{R}(s,t)\,\mathbf{E}(s,t),$$
$$\mathbf{E}(s,s) = \mathbf{I}. \tag{3.35}$$

The interpretation of the above equation is that the change in $\mathbf{E}$ is equal to the deformation of $\mathbf{E}$ caused by the objective rate $\mathbf{R}$. The numeric approximation of the derivative of $\mathbf{E}$ in (3.35) is,

$$\frac{\partial \mathbf{E}(s,t)}{\partial t} \approx \frac{\tilde{\mathbf{E}} - \mathbf{I}}{k}, \tag{3.36}$$

where $\tilde{\mathbf{E}}$ is the approximate solution to the ODE. Then,

$$\tilde{\mathbf{E}}(s,t) = (\mathbf{I} - k\mathbf{R}(s,t))^{-1}. \tag{3.37}$$

After solving for the approximation solution $\tilde{\mathbf{E}}$ and substituting this result back into (3.34) the numeric representation of the Lie derivative becomes,

$$\varphi\frac{\boldsymbol{\zeta} - \tilde{\mathbf{E}}\boldsymbol{\zeta}(t-k,t)\,\tilde{\mathbf{E}}^T}{k} + \alpha\boldsymbol{\zeta} = \beta I. \tag{3.38}$$

Finally, note that $\mathbf{x}(t-k)$ is the spatial position, back in time, of a parcel of fluid, i.e., a departure foot. Then the notation for the departure feet, $\tilde{\mathbf{y}}$, can be

introduced into (3.38). Having already development the solution for $\tilde{\mathbf{y}}$ the notation is used below without further discussion. The resulting expression is,

$$\varphi\frac{\boldsymbol{\zeta}-\tilde{\mathbf{E}}\boldsymbol{\zeta}\left(\tilde{\mathbf{y}}\right)\tilde{\mathbf{E}}^{T}}{k}+\alpha\boldsymbol{\zeta}=\beta\mathbf{I}. \tag{3.39}$$

The solution to the above is,

$$\boldsymbol{\zeta}=\frac{1}{\varphi+k\alpha}\left(\varphi\tilde{\mathbf{E}}\boldsymbol{\zeta}\left(\tilde{\mathbf{y}}\right)\tilde{\mathbf{E}}^{T}+k\beta\mathbf{I}\right). \tag{3.40}$$

where $\boldsymbol{\zeta}\left(\tilde{\mathbf{y}}\right)$ is assumed to be known as it is a quantity (in our case stress) evaluated at a past time. One should note that this solution exists even when $\varphi=0$. The solution for $\boldsymbol{\zeta}$ when $\varphi=0$ is

$$\boldsymbol{\zeta}=\frac{\beta}{\alpha}\mathbf{I}. \tag{3.41}$$

For the Oldroyd-B stress model this means that the elastic stress is zero because of the definition of the conformation stress, (2.39).

Only three distinct values for the second order tensor $\boldsymbol{\zeta}$ need to be determined because $\boldsymbol{\zeta}$ is symmetric, namely $\boldsymbol{\zeta}_{1,2}=\boldsymbol{\zeta}_{2,1}$. These solutions can be determined locally because the stress at one physical position at time t_n does not depend on another physical position at time t_n. Recall that the solution does depend upon the stress at another physical position at time t_{n-1} and this is called the departure foot, but it is known and so is the stress at this point in space and time.

Now, for the Oldroyd-B model $\mathbf{R}=\nabla\mathbf{u}$ in which case $\mathbf{E}$ is very similar to (3.11) and it can be shown that

$$\tilde{\mathbf{E}}=\frac{1}{1+k\mathrm{tr}(\nabla\mathbf{u})+k^{2}\det(\nabla\mathbf{u})}(\mathbf{I}-k\det(\nabla\mathbf{u})(\nabla\mathbf{u})^{-1}). \tag{3.42}$$

By denoting the inverse of the gradient of $\mathbf{u}$, defined in (3) as $\mathbf{A_u}$, substituting $\boldsymbol{\zeta} = \mathbf{c}$ and the solution for $\tilde{\mathbf{E}}$, (3.42) into equation (3.40) it can be shown that,

$$\mathbf{c} = \frac{1}{\varphi + k\alpha}[\frac{\varphi}{\left(1 + k\text{tr}(\nabla\mathbf{u}) + k^2\text{det}(\nabla\mathbf{u})\right)^2}(\mathbf{c}\left(\tilde{\mathbf{y}}\right) - \mathbf{c}\left(\tilde{\mathbf{y}}\right)\mathbf{A_u}^T - \mathbf{A_u}\mathbf{c}\left(\tilde{\mathbf{y}}\right) + \mathbf{A_u}\mathbf{c}\left(\tilde{\mathbf{y}}\right)\mathbf{A_u}^T) + k\beta\mathbf{I}]. \tag{3.43}$$

By substituting the definition of the conformation stress (2.39) into the above yields,

$$\boldsymbol{\tau} = \frac{1}{\varphi + k\alpha}[\frac{\varphi}{\left(1 + k\text{tr}(\nabla\mathbf{u}) + k^2\text{det}(\nabla\mathbf{u})\right)^2}(\mathbf{c}\left(\tilde{\mathbf{y}}\right) - \mathbf{c}\left(\tilde{\mathbf{y}}\right)\mathbf{A_u}^T - \mathbf{A_u}\mathbf{c}\left(\tilde{\mathbf{y}}\right) + \mathbf{A_u}\mathbf{c}\left(\tilde{\mathbf{y}}\right)\mathbf{A_u}^T) + k\beta\mathbf{I}] - \frac{\eta_p}{\text{Wi}}\mathbf{I}. \tag{3.44}$$

In summary, having shown that the Lie derivative is consistent with a SMRDE a numeric solution has been developed based on the solution to the SMRDE. This solution can be found [31].

Advection:

The same FEM techniques are applied to the advection equation,

$$\frac{\partial\varphi}{\partial t} + \mathbf{u}\nabla\varphi = \nabla\cdot\left(D_{\text{coeff}}\varphi\nabla\varphi\right), \tag{3.45}$$

which models the evolution of the biofilm volume fraction, φ. The biofilm volume fraction is approximated using quadratic basis functions with 2D thirteen point Gaussian quadrature in the elements and 1D four point Gaussian quadrature on the boundary. The weights and barycentric coordinates can be found in Tables 2.3 and 2.4. Diffusion has been introduced into the advection equation to stabilize

the numerics. The diffusion coefficient D_{coeff} has been scaled by the biofilm volume fraction to further reduce the artificially introduced diffusion. This change effectively decreases the diffusion rate as the biofilm volume fraction reduces. In this way the diffusion coefficient is coupled with the biofilm volume fraction and so there is no diffusion where there is no biofilm. In order to further increase the stability of the numerics the Galerkin Least Squares (GLS) method, which is discussed in the introduction, has been employed. The weak form for (2.7) is,

$$\left(b_e, \frac{\varphi_e^{\text{new}}}{k}\right) + D_{\text{coeff}}\varphi_e^{\text{old}}\left(\nabla b_e : \nabla\varphi_e^{\text{new}}\right) + \left(b_e, \mathbf{u}_e^{\text{old}} \cdot \nabla\varphi_e^{\text{new}}\right) = \left(b_e, \frac{\varphi_e^{\text{old}}}{k}\right). \tag{3.46}$$

The GLS term is

$$\int_e \tau_{GLS}\left(\frac{b_e}{k} + \mathbf{u}_e^{\text{old}} \cdot \nabla b_e\right)\left(\frac{\partial\varphi_e}{\partial t} + \mathbf{u}_e^{\text{old}} \cdot \nabla\varphi_e^{\text{new}}\right), \tag{3.47}$$

where τ_{GLS} is the so called, intrinsic time parameter. In this work τ_{GLS} has been set equal to one. However, the intrinsic time parameter should really be modeled by a more complicated expression. Unfortunately, the exact form of this equation, for higher dimensions, is still an open question [4, 11]. After applying the GLS method to the advection equation we arrive at the following weak form,

$$\begin{aligned}&\left(b_e, \frac{\varphi_e^{\text{new}}}{k}\right) + D_{\text{coeff}}\varphi_e^{\text{old}}\left(\nabla b_e : \nabla\varphi_e^{\text{new}}\right) + \left(b_e, \mathbf{u}_e^{\text{old}} \cdot \nabla\varphi_e^{\text{new}}\right)\\ &+ \tau_{GLS}\left(\frac{b_e}{k} + \mathbf{u}_e^{\text{old}} \cdot \nabla b_e, \frac{\left(\varphi_e^{\text{new}} - \varphi_e^{\text{old}}\right)}{k} + \mathbf{u}_e^{\text{old}} \cdot \nabla\varphi_e^{\text{new}}\right) = \left(b_e, \frac{\varphi_e^{\text{old}}}{k}\right),\end{aligned} \tag{3.48}$$

where φ_e^{old} and $\mathbf{u}_e^{\text{old}}$ are the known biofilm volume fraction and velocity, respectively, at the current time step. It should be noted that "old" velocities are not evaluated at departure feet when numerically solving the advection equation.

The elements of the global matrix and right hand side for the biofilm volume fraction advection equation finite element approximation are as follows,

$$\begin{aligned}[\mathbf{A}]_{i,j} = &\int_e \varphi_i\varphi_j + \varphi^{\text{old}} D_{\text{coeff}} k \left(\frac{\partial\varphi_i}{\partial x}\frac{\partial\varphi_j}{\partial x} + \frac{\partial\varphi_i}{\partial y}\frac{\partial\varphi_j}{\partial y} \right) \\ &+ k\varphi_i \left(u_{1,e}^{\text{old}} \frac{\partial\varphi_j}{\partial x} + u_{2,e}^{\text{old}} \frac{\partial\varphi_j}{\partial y} \right) \\ &+ \tau_{\text{GLS}} k \left(\frac{\varphi_i}{k} + \frac{\partial\varphi_i}{\partial x} u_{1,e}^{\text{old}} + \frac{\partial\varphi_i}{\partial y} u_{2,e}^{\text{old}} \right) \left(\frac{\varphi_j}{k} + \frac{\partial\varphi_j}{\partial x} u_{1,e}^{\text{old}} + \frac{\partial\varphi_j}{\partial y} u_{2,e}^{\text{old}} \right) \text{dA}, \end{aligned} \tag{3.49}$$

$$[\mathbf{F}]_i = \int_e \varphi^{\text{old}}\varphi_i + \tau_{\text{GLS}}\varphi^{\text{old}} \left(\frac{\varphi_i}{k} + u_{1,e}^{\text{old}} \frac{\partial\varphi_i}{\partial x} + u_{2,e}^{\text{old}} \frac{\partial\varphi_i}{\partial y} \right) \text{dA}, \tag{3.50}$$

where the size of $\mathbf{A}$ is N_{Quad} by N_{Quad} and the length of $\mathbf{F}$ is N_{Quad}.

These are the numeric methods which produced the results that are discussed in the next chapter. The numeric solutions to this model have proven to be incredibly stable. However, for large time step values the departure foot numeric method does eventually fail, but even with these defective departure foot values the rest of the numeric methods continue to converge for some time. In Chapter 4, this single instance of instability is documented and discussed. The results of the model for a variety of initial biofilm configurations and surfaces for both velocities, the pressure, the three stress components as well as a few interesting computations that describe biofilm dynamics are presented in the next chapter.

RESULTS

The results from this model are very promising. The predicted behavior agrees quite well with expected behavior given simple assumptions about the nature of fluid flow. The 2-D plots for the horizontal and vertical velocity, pressure and three stress components are presented for a reference initial biofilm profile. The 2-D plots for results with a variety of different initial biofilm volume fraction surfaces are shown. The quality with which the model satisfies the fundamental assumptions made during the model development are shown by computation and illustrated graphically. The assumption that $\mathbf{u}\nabla\mathbf{u} = 0$ is shown to be closely satisfied. The incompressibility condition $\nabla \cdot \mathbf{u} = 0$ is graphed. The rotation of the fluid is described by graphing the z-component of $\nabla \times \mathbf{u}$. The common parameters used for all simulations, except where otherwise stated, are listed Table 4.1.

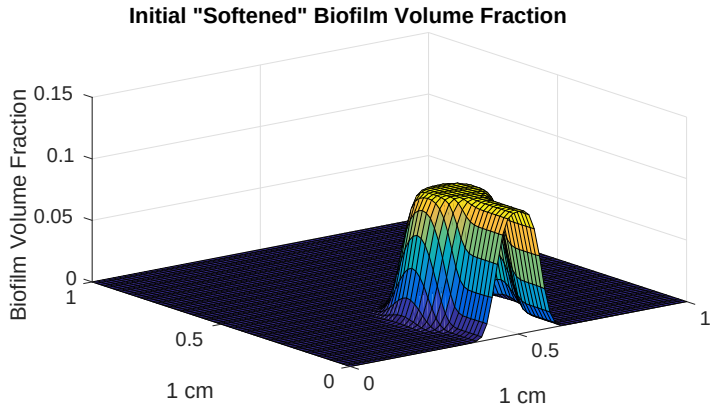
Parameter List		
Parameter	Value	Units
Spatial Step Size, $\triangle x$	1.0 / 32.0	cm
Time Step	$0.1\triangle x$	sec
Solvent Viscosity	1.0	Pa·sec
Biofilm Viscosity	500.0	Pa·sec
Relaxation Time	120.0	sec
Solvent Density	1.0	kg/m^3
Biofilm Density	1.0	kg/m^3
Time Scale	60.0	sec
Length Scale	0.01	m
Diffusion Coefficient	10^{-5}	m^2/sec
Johnson-Segalman Parameter	1.0	

Table 4.1: List of parameters used in most simulations

Results:

Most of the following results are presented on a 64 triangular element per row by 32 row grid. This relatively small mesh size is used to keep computation time relatively low. The results section begins with a presentation of the lone instability that has been discovered, that is, the hidden CFL type condition is attributed to the numeric solution for the departure feet. However, before the surface showing some of the errors caused by violating the CFL type condition is shown, the initial biofilm surface, used for most of the following results, is reshown shown in Figure 4.1.

Figure 4.1: The initial biofilm volume fraction after diffusion softening.

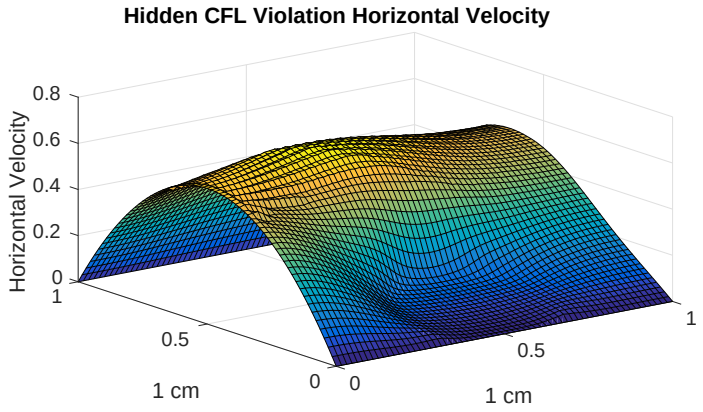


This surface in Figure 2.5 is the result of diffusing the initial sharp biofilm surface shown.

Hidden CFL-type Problem:

The hidden CFL type problem first appeared when the maximum inflow velocity was set equal to one and a time step value much greater than one one hundredth of the spatial step size was used. It was discovered that when a time step size exceeded $0.01\triangle x$ then oscillations occurred on the peak in the horizontal velocity, as can be

Figure 4.2: After 15 time steps instability appears.



seen in Figure 4.2. This peak is formed when the solvent flows over the top of the biofilm. The biofilm causes a reduction in the cross section of the pipe and and thus, as a result of the incompressibility condition, the fluid velocity must increase. Shortly after the formation of these oscillations begins, the departure foot algorithm ceases to converge and subsequently the entire algorithm no longer proceeds.

In Figure 4.2 the oscillations caused by violating the CFL condition show up after 15 times steps. The departure foot algorithm failed to converge after 23 time steps. This failure is attributed to the finite element method producing results with discontinuous derivatives. Since the departure foot algorithm depends directly upon the gradient of the velocity, this lack of continuity is catastrophic if a departure foot leaves its original element. This is the likely cause of the hidden CFL condition. This assumption has been validated by checking if a departure foot has left its element. In every single stable result the departure foot has not left its original element. In the results wherein the CFL condition has been violated, the departure foot has left its original element.

Velocity:

The velocity has two components, horizontal and vertical and are presented separately. There are a few important computations which can be made using these velocities. The vorticity, $\nabla \times \mathbf{u}$, incompressibility, $\nabla \cdot \mathbf{u}$, and the size of the inertia term, $\mathbf{u}\nabla\mathbf{u}$ are all computed using velocities but are presented in separate sections of the results chapter.

Horizontal Velocity:

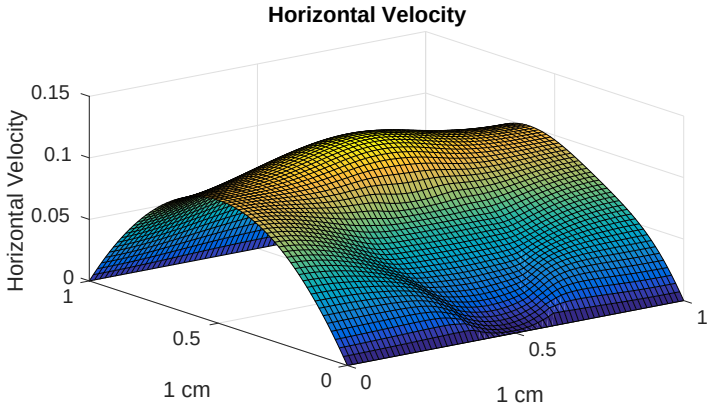
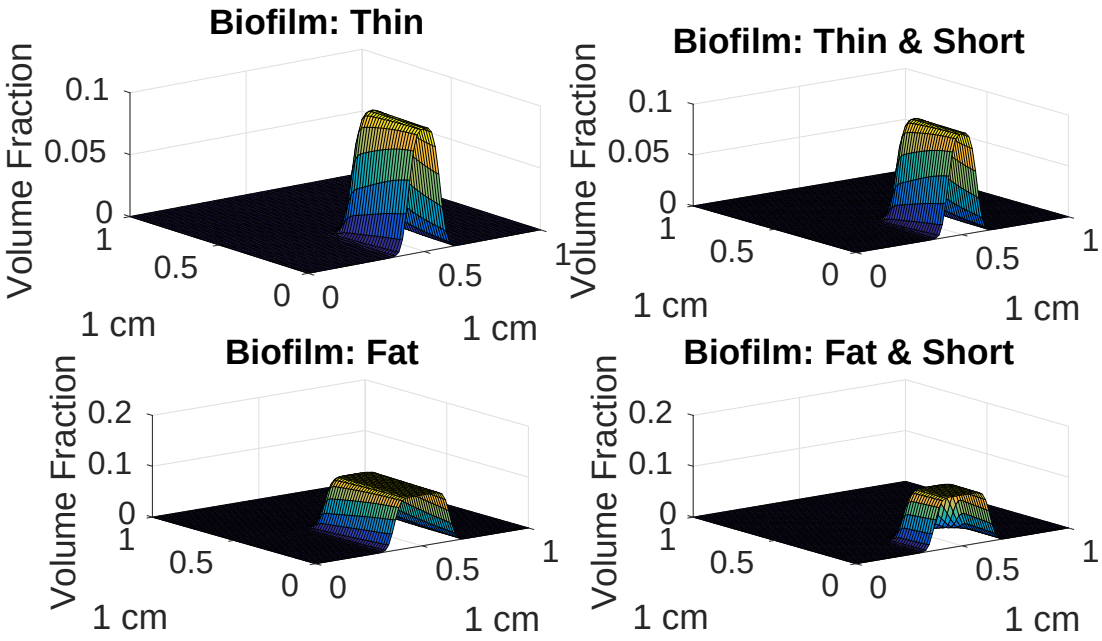


Figure 4.3: Horizontal velocity bulb biofilm in the middle of the domain at the 100th time step.

The speed of the horizontal velocity increases as the solvent flows over the top of the biofilm, Figure 4.3. This increase is attributed to the effective restriction in the diameter of the cross section of pipe caused by the biofilm. A shorter biofilm profiles show a significant reduction in horizontal flow, within the biofilm. While a taller biofilm profiles exhibit a more pronounced horizontal velocity. This difference in behavior is considered a result of the taller biofilms picking up velocity from the middle of the pipe and the incompressibility condition causing the transfer of horizontal

velocity through the rest of the biofilm. Shorter biofilms are not exposed to the higher speed flow in the middle of the pipe and therefore do not speed up as much as their taller counterparts. Figure 4.5 shows surfaces for the horizontal velocities, after 100 timesteps, for short, tall, fat and thin initial biofilm volume fraction surfaces. The corresponding initial biofilm volume fraction surfaces are first shown in Figure 4.4.

Figure 4.4: Four different initial biofilm surfaces.

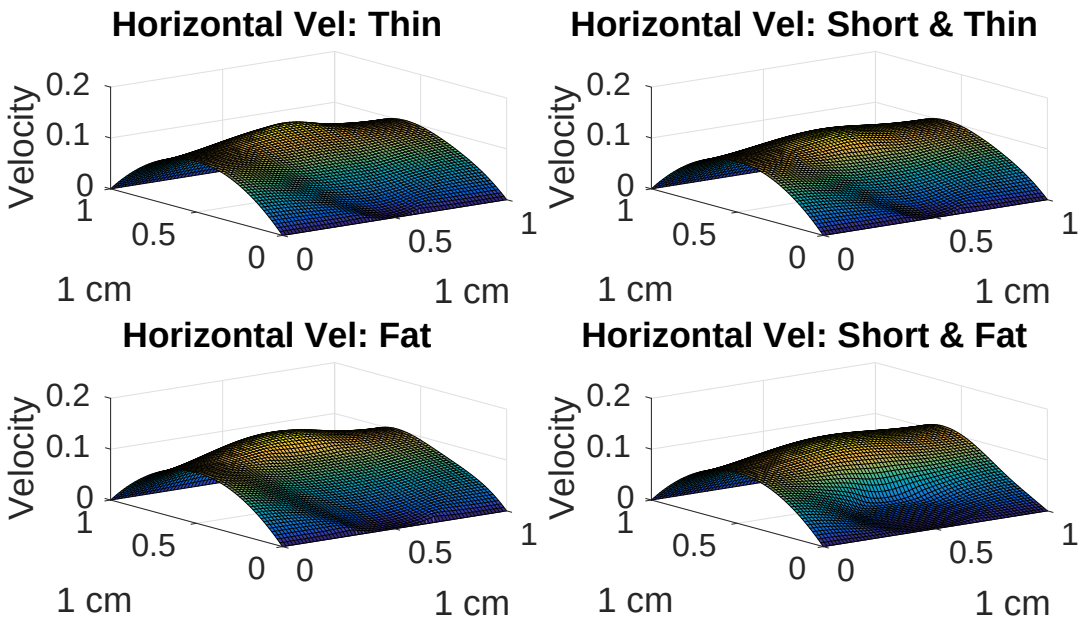


The shortest and widest initial biofilm volume fraction has the lowest increase in horizontal velocity while the tallest and thinest biofilm has the greatest increase.

Vertical Velocity:

The vertical velocity surface in Figure 4.6 shows a positive flow in front of the biofilm and a negative flow behind the biofilm. This is consistent with the less viscous

Figure 4.5: Horizontal velocities comparing short, tall, fat and thin horizontal velocity surfaces after 100 time steps.



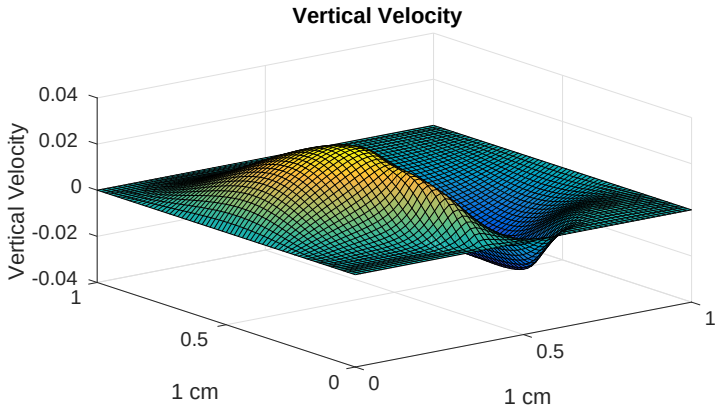
fluid flowing up, over, and then down behind the much more viscous biofilm. This behavior shows an expected flow characteristic for the purely viscous solvent.

After removing the entry boundary flow, and after waiting a hundred or so time steps, both the horizontal and the vertical velocities reduce by several orders of magnitude, as shown in Figure 4.7, from their maximum values. At this point it is reasonable to assume that the system is at quasi-equilibrium.

Pressure:

The spikes in the pressure surface, Figure 4.8 are not considered instabilities. The spikes are believed to be caused by a lack of resolution. Overall, an understanding of the pressure in a biofilm whose base is attached to the bottom of the domain while

Figure 4.6: Vertical velocity bulb biofilm in the middle of the domain at the 100th timestep.

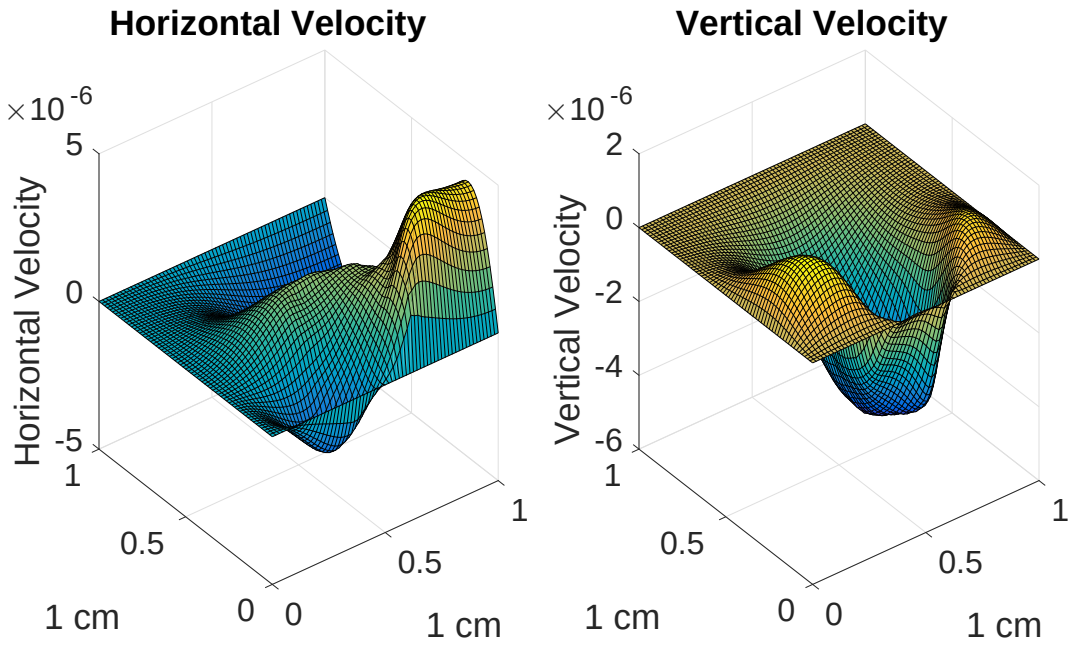


being sheared by water flow is captured by this image. As the biofilm is sheared off of the base of the pipe by the solvent, the biofilm will form a negative pressure in the leading edge and a positive pressure on the back edge. The negative pressure is assumed to be caused by the biofilm suctioning onto the wall to compensate for the solvent shearing it away from the wall. While the positive pressure is likely caused by the biofilm pushing against itself as it is pushed into the wall. Different biofilm profiles exhibit different responces to shear.

If one begins with a flat initial biofilm volume fraction surface, as in Figure 4.9, then the pressure behavior is somewhat different. A "flat" biofilm profile could be thought of as the result of a larger biofilm which has detached from itself leaving just a small amount of material behind on the wall.

A low profile biofilm does not exhibit the large pressure spikes seen in the bulb pressure surface. See Figure 4.10 for the pressure predicted by the model after 100 time steps given a flat initial biofilm. However, there does appear to be oscillations on the lower boundary. It should be noted that, on the first half, the pressure inside the biofilm is still less than the external pressure. As a result, the leading edge of

Figure 4.7: Horizontal and vertical velocity bulb biofilm in the middle of the domain after 170 time steps.



the biofilm is still being suctioned to the wall of the pipe and then pushing back on the back side of the biofilm. This behavior is consistent with what has already been presented.

This is an important result as it suggests that increasing flow is not likely to cause the complete removal of a biofilm. Of more interest numerically is the effect of refining the mesh grid. When a 128 elements per row by 64 row grid is used the pressure profile changes somewhat and suggests that the true behavior is more dramatic than that which is suggested by the coarse grid. When the grid is further refined to 256 elements per row with 128 rows the behavior changes remarkably. In figure 4.11, this dramatic change is presented. This suggests that the model is capable of capturing steep changes and that the mesh size is the limiting factor in capturing these structures in both the flat biofilm and the bulb biofilm. It should be noted that

Figure 4.8: Pressure bulb biofilm in the middle of the domain at the 100th time step.

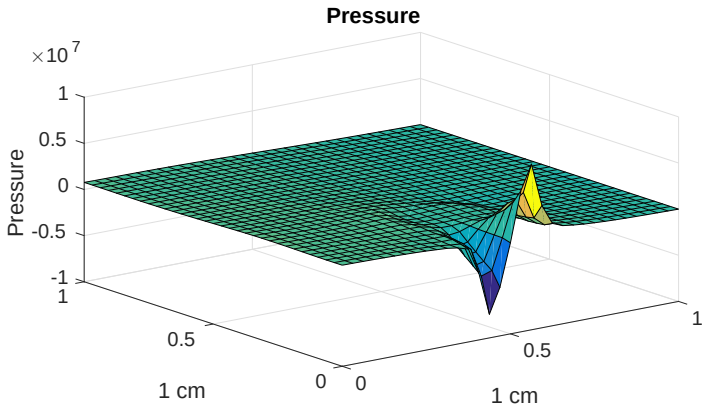
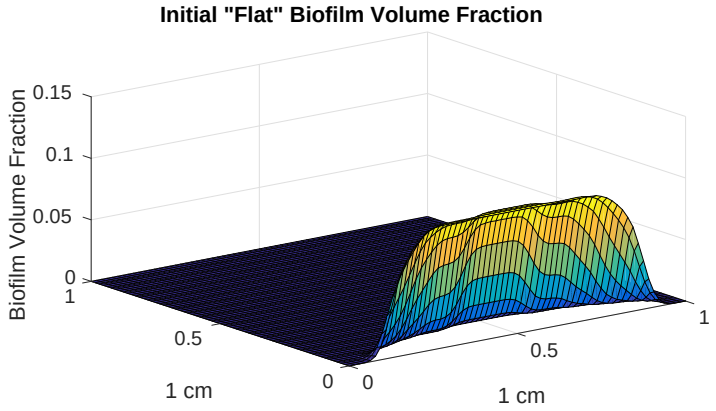


Figure 4.9: Flat initial biofilm.

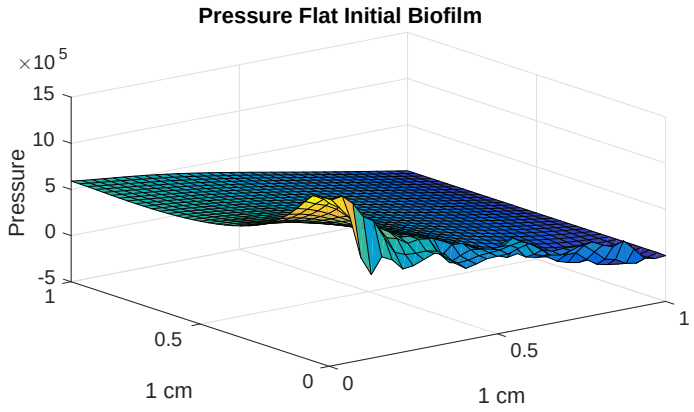


the negative pressure on the leading edge and positive pressure on the back edge is still evident.

Stress:

The stress has three components. The first is the stress in the horizontal direction perpendicular to a vertical plane. The second is the stress in the vertical direction perpendicular to a horizontal plane. The third is the stress in the vertical direction on a vertical plane which is equivalent to the stress in the horizontal direction on a

Figure 4.10: Pressure surface at 100th time step for a flat initial biofilm.



horizontal plane, hence the symmetry of the stress tensor is a physical requirement as well as a mathematical requirement.

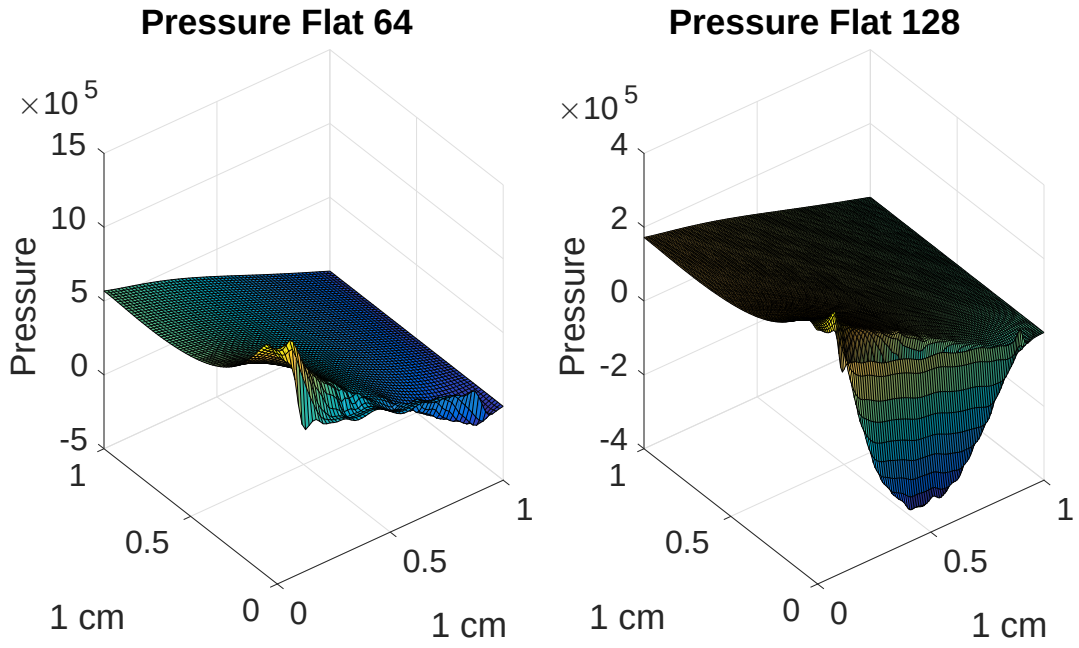
XX-Stress Component:

The depression where the biofilm resides, which can be seen in Figure 4.12, is attributed to the high biofilm elasticity resisting movement. The flatfeature surrounding the depression, is the result of the lack of biofilm, and the definition of the conformation stress, (2.39). The conformation stress is the elastic stress shifted up and therefore, this is where there is no elastic stress.

XY-Stress Component:

The shearing elastic stress is captured by the XY-component in Figure 4.13. There is a noticeable asymmetry in this surface. This is attributed to the flow across the biofilm which is itself asymmetric. One should note that there is a drop in elastic shear stress in the middle of the biofilm stalk. This drop in shear stress in the middle

Figure 4.11: Pressure surface mesh grid refinement at 100th time step for a flat initial biofilm.



of the stalk seems reasonable, and it is assumed that the biofilm protects itself from the external shear stress imparted by the solvent.

YY-Stress Component:

This ddepression where the biofilm is located in Figure 4.14 looks very much like that which is shown in the XX-component but it is in fact slightly different. However the mechanism for its formation is assumed to be the same as that for the XX-component.

Figure 4.12: Stress XX bulb biofilm in the middle of the domain at the 100th time step.

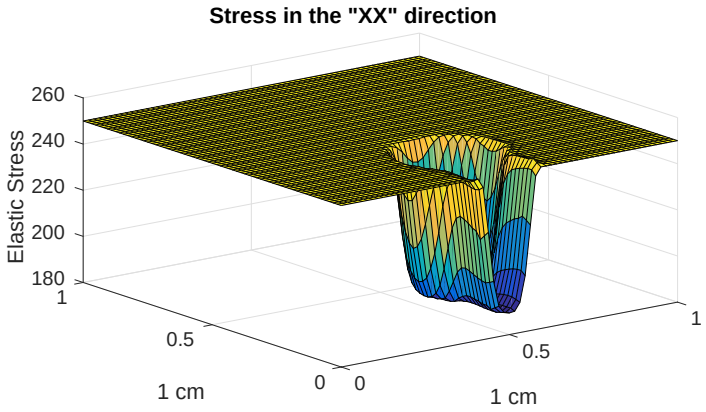
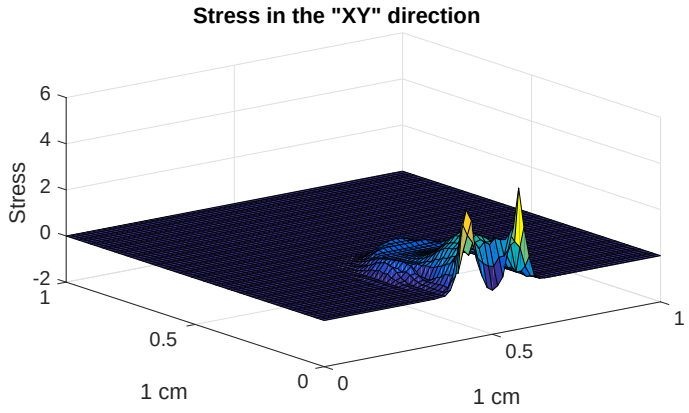


Figure 4.13: Stress XY bulb biofilm in the middle of the domain at the 100th time step.



Incompressibility:

In Figure 4.15 shows the incompressibility condition is not perfectly preserved but, for most of the surface, is several orders of magnitude smaller than the maximum velocity. The spike on the lower left corner of the biofilm is not understood but is attributed to the biofilm being compressed by the rotation caused by the shear stress imparted by the solvent flow. The derivatives were computing using forward Euler.

Figure 4.14: Stress YY bulb biofilm in the middle of the domain at the 100th time step.

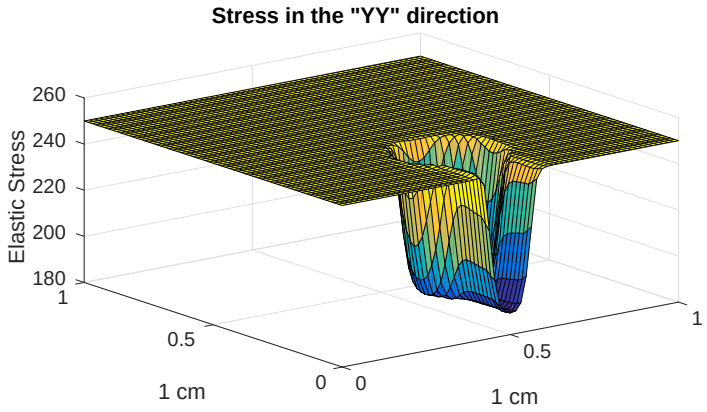
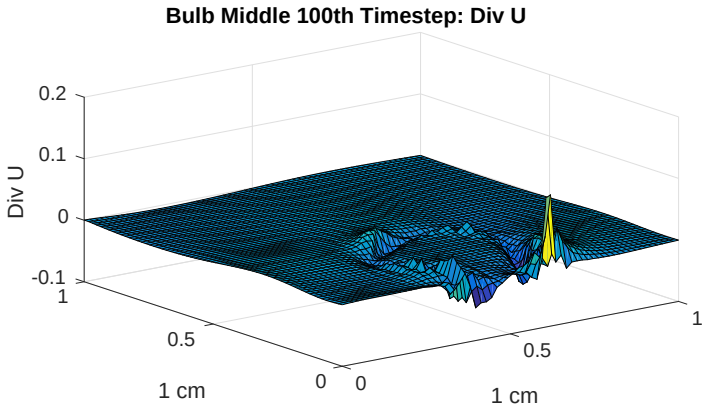


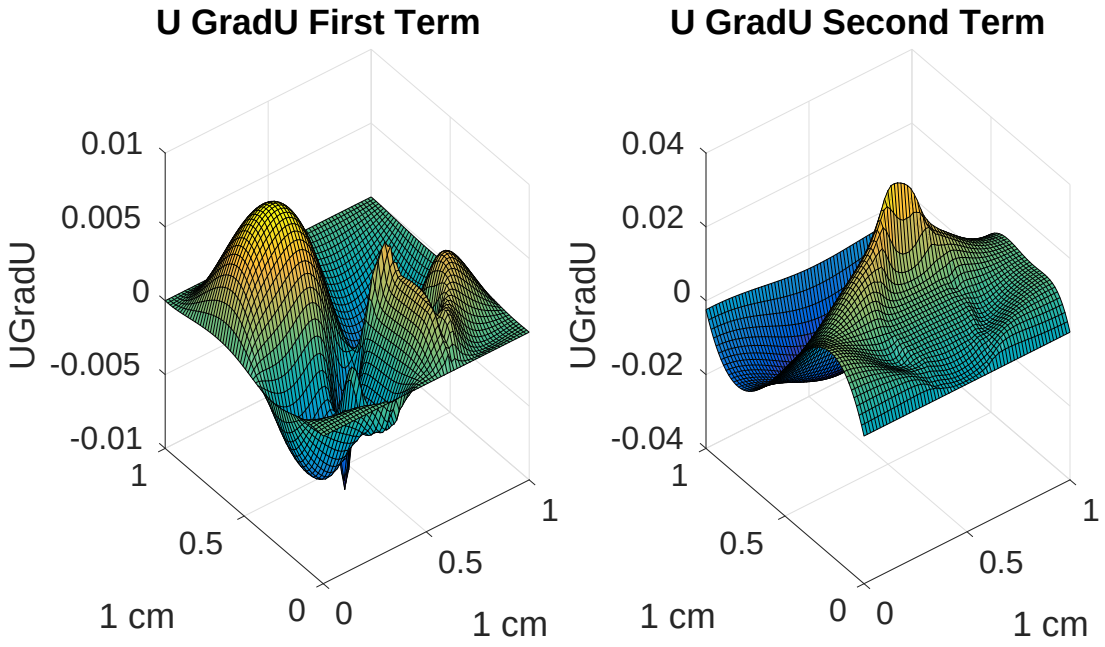
Figure 4.15: Numeric approximation of $\nabla \cdot \mathbf{u}$ at the 100th time step.



Non-linesar Inertia Term: $\mathbf{u}\nabla\mathbf{u}$

As shown in Figure, 4.16 the size of the $\mathbf{u}\nabla\mathbf{u}$ is several orders of magnitude smaller than the maximum velocity and confirms that removing this term is a reasonable assumption. Again, the derivatives were computed using forward Euler.

Figure 4.16: Numeric approximation of $\mathbf{u}\nabla\mathbf{u}$ at the 100th time step.

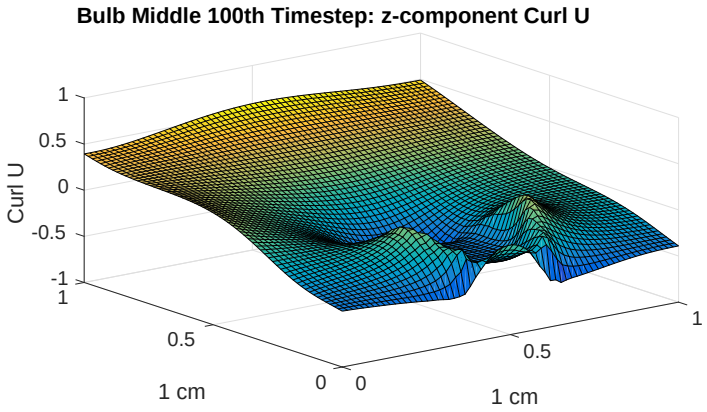


Vorticity:

Vorticity is demonstrated by computing the curl of the velocity, $\nabla \times \mathbf{u}$ and plotted the z-component of the curl. The surface for the curl of a biofilm with an initial bulb in the middle of the domain, after 100 time steps, is shown in Figure 4.17. In Figure 4.17 we see that most values are non-zero. Hence the fluid is rotating. Using the right hand rule, the polymer is rotating clockwise and the solvent flowing over the top of the polymer is rotating counter clockwise. There are small regions under the bulb and next the the stalk where the fluid is rotating counter clockwise.

From the "right hand rule" this Figure 4.17 illustrates the clockwise rotation of the base of the biofilm which was inferred by the pressure surface. The derivatives where approximated using forward Euler.

Figure 4.17: Z-component of the curl of the velocity after 100 time steps, computed using forward Euler.



The model contains a number of parameters. Identifying which parameters effect the results and by how much is an important part of analyzing the model. In the next section results comparing the effects of changing a few parameter values are displayed.

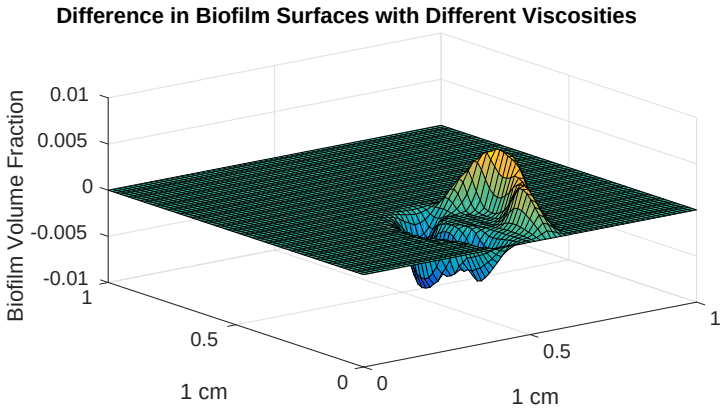
Parameter Variations:

The first parameter which is varied is the viscosity of the biofilm to water ratio. Next the GLS stabilizing parameter is varied. Finally, variations to the Johnson-Segalman parameter are then explored.

Biofilm Viscosity:

Reducing the viscosity of the biofilm causes more flow in the biofilm with the same solvent velocity. In Figure 4.18 the biofilm surface with a viscosity of 500 was subtracted from a biofilm surface with a viscosity of 50, after 100 time steps. Clearly the less viscous fluid has flowed more than the more viscous fluid.

Figure 4.18: The difference in biofilm surfaces with different viscosities after 100 time steps.



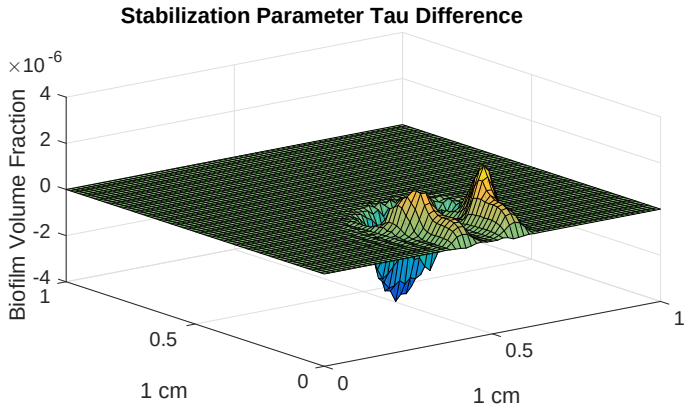
GLS:

The GLS stabilization parameter τ_{GLS}, which is called the intrinsic time [11], has no optimal definition [11], for higher dimensional models. With this in mind τ_{GLS} was set equal to 1.0 for all of the results except those shown in Figure 4.19. In [46] a value of 0.3 was used. Since the original motivation for using the GLS came from that paper a simulation was run using this value. The variation in biofilm surfaces was on the order of 10^{-6}. Hence the τ_{GLS} value has little impact on stability or the model predictions.

Johnson-Segalman:

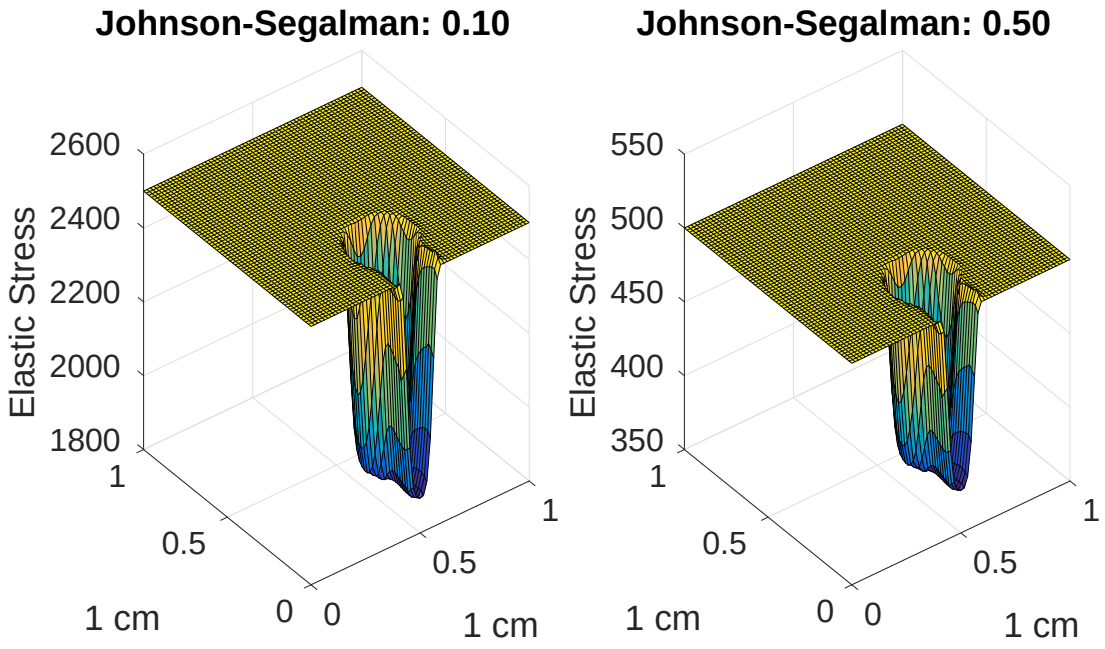
The slippage parameter in the Johnson-Segalman model a has been tested for different values in Figure 4.20. Consistent with the original development negative values of a do not yield good results [24, 31]. The only impact is a direct scaling of the stress components but with no overall change in stress behavior.

Figure 4.19: GLS stabilization parameter.



The inconsistency of the incompressibility condition appears to be within an acceptable range. The pressure scale is quite large. While this is concerning it suggest that parameter values still need to be adjusted. At this time using this model to make meaningful predictions about biofilm behavior would be a significant leap. However, one could conclude that using a symmetry preserving numeric scheme for modeling the elastic stress tensor for a biofilm in an inhomgeneous flow is at the very least, viable. In summary, the results are quite promising.

Figure 4.20: Johnson-Segalman slippage parameter.



CONCLUSION

A novel inhomogeneous viscoelastic 2D fluid flow model that preserves the symmetry of the numeric representation of the stress tensor has been developed. In this work it has been shown how the work in [30,31] can be extended to inhomogeneous fluid flows. The Navier-Stokes model has then been coupled with an advection equation, applied to the biofilm volume fraction. The inhomogeneity of the described fluid created a subtle variation in the solution developed in [30, 31] and a method has been introduced to numerically address this complication. The Galerkin least squares method was applied to the advection model to increase its stability. In order to solve this coupled system in a reasonable amount of time, the Trilinos sparse matrix solver library AztecOO was used in conjunction with the message passing interface (MPI) and implemented in C++.

Due to the scale of this problem, parallel processing is necessary. Parallel processing was implemented using an architecture called MPI. The solver package AztecOO presented some interesting coding challenges. In order to effectively use MPI local cpu memory as well as global RAM memory must be managed. As a necessity, memory maps have been used to add and remove data from local memory stacks.

The motivation for this work is to increase understanding of biofilms due to the myriad ways in which biofilms benefit and harm society. The costs associated with infected implants and contaminated pipes as well as the benefits of cheap fuel and clean water cannot be overstated.

There have been numerous attempts to measure biofilm flow characteristics. While these have been successful, the use of a mathematical model can give more insight. The presented results show some of the ways in which additional mechanical

values could be estimated. For example, the internal stresses of a biofilm have been estimated without scraping the biofilm off of the surface to which it had attached and grown.

In the future, adding an attachment/detachment model to this work could be used to determine under which conditions a biofilm will detach from itself, having exceeded some internal stress threshold. Given a growth model, long term growth characteristics could be predicted. The mechanical information predicted by the presented model could be used to suggest methods for biofilm removal, and further, which methods are likely to be the most successful. The most efficient removal practices will minimize stresses placed on equipment used to remove biofilms. By including the elastic stress inside a biofilm detachment may be more accurately predicted. While the current work does not include a detachment parameter, where the predicted stresses exceed some threshold, detachment can be inferred. In addition, the minimum flow which induces this detachment could be determined. However, this model suggests that a biofilm is unlikely to be completely removed from a surface to which it has attached by simply increasing the flow over the top of it.

REFERENCES CITED

[1] Erik Alpkvista and Isaac Klapper. A multidimensional multispecies continuum model for heterogeneous biofilm development. *Bulletin of mathematical biology*, 69(2):765–789, 2007.

[2] Carla Renata Arciola, Davide Campoccia, Pietro Speziale, Lucio Montanaro, and John William Costerton. Biofilm formation in staphylococcus implant infections. a review of molecular mechanisms and implications for biofilm-resistant materials. *Biomaterials*, 33(26):5967–5982, 2012.

[3] Frank Baaijems. An u-ale formulation of 3-d unsteady viscoelastic flow. *International Journal for Numerical Methods in Engineering*, 36(7):1115–1143, 1993.

[4] Alexander N Brooks and Thomas JR Hughes. Streamline upwind/petrov-galerkin formulations for convection dominated flows with particular emphasis on the incompressible navier-stokes equations. *Computer methods in applied mechanics and engineering*, 32(1):199–259, 1982.

[5] Ron Buckmire. Application of a mickens finite-difference scheme to the cylindrical bratu-gelfand problem. *Numerical Methods for Partial Differential Equations*, 20(3):327–337, 2004.

[6] HR Bungay, WJ Whalen, and WM Sanders. Microprobe techniques for determining diffusivities and respiration rates in microbial slime systems. *Biotechnology and Bioengineering*, 11(5):765–772, 1969.

[7] William G Characklis and Kevin C Marshall. Biofilms. 1990.

[8] Stephen Childress. *An introduction to theoretical fluid mechanics*, volume 19. American Mathematical Soc., 2009.

[9] NG Cogan. Two-fluid model of biofilm disinfection. *Bulletin of mathematical biology*, 70(3):800–819, 2008.

[10] JM Dealy. Weissenberg and deborah numberstheir definition and use. *Rheol. Bull*, 79(2):14–18, 2010.

[11] Jean Donea and Antonio Huerta. *Finite element methods for flow problems*. John Wiley & Sons, 2003.

[12] Gianfranco Donelli. Biofilm-based healthcare-associated infections. *Advances in Experimental Medicine and Biology*, 2015.

[13] Jim Douglas, Jr and Thomas F Russell. Numerical methods for convection-dominated diffusion problems based on combining the method of characteristics with finite element or finite difference procedures. *SIAM Journal on Numerical Analysis*, 19(5):871–885, 1982.

[14] François Dupret, JM Marchal, and MJ Crochet. On the consequence of discretization errors in the numerical calculation of viscoelastic flow. *Journal of non-newtonian fluid mechanics*, 18(2):173–186, 1985.

[15] Raanan Fattal and Raz Kupferman. Time-dependent simulation of viscoelastic flows at high weissenberg number using the log-conformation representation. *Journal of Non-Newtonian Fluid Mechanics*, 126(1):23–37, 2005.

[16] Michel Fortin. An analysis of the convergence of mixed finite element methods. *RAIRO-Analyse numérique*, 11(4):341–354, 1977.

[17] Charles J Gantzer, Bruce E Rittmann, and Edwin E Herricks. Mass transport to streambed biofilms. *Water Research*, 22(6):709–722, 1988.

[18] William M Gelbart and Avinoam Ben-Shaul. The new science of complex fluids. *The Journal of Physical Chemistry*, 100(31):13169–13189, 1996.

[19] Luanne Hall-Stoodley, J William Costerton, and Paul Stoodley. Bacterial biofilms: from the natural environment to infectious diseases. *Nature reviews microbiology*, 2(2):95–108, 2004.

[20] Luanne Hall-Stoodley and Paul Stoodley. Biofilm formation and dispersal and the transmission of human pathogens. *Trends in microbiology*, 13(1):7–10, 2005.

[21] Harald Horn and Susanne Lackner. Modeling of biofilm systems: a review. In *Productive Biofilms*, pages 53–76. Springer, 2014.

[22] A Houari, J Picard, H Habarou, L Galas, H Vaudry, V Heim, and P Di Martino. Rheology of biofilms formed at the surface of nf membranes in a drinking water production unit. *Biofouling*, 24(4):235–240, 2008.

[23] Ilia Y Jimenez and Richard Bartha. Solvent-augmented mineralization of pyrene by a mycobacterium sp. *Applied and Environmental Microbiology*, 62(7):2311–2316, 1996.

[24] MW Johnson and D Segalman. A model for viscoelastic fluid behavior which allows non-affine deformation. *Journal of Non-Newtonian fluid mechanics*, 2(3):255–270, 1977.

[25] Roland Keunings. A survey of computational rheology. In *Proceedings of the XIIIth International Congress on Rheology*, volume 1, pages 7–14. Citeseer, 2000.

[26] Isaac Klapper and Jack Dockery. Mathematical description of microbial biofilms. *SIAM review*, 52(2):221–265, 2010.

[27] Isaac Klapper, CJ Rupp, R Cargo, B Purvedorj, and P Stoodley. Viscoelastic fluid description of bacterial biofilm material properties. *Biotechnology and Bioengineering*, 80(3):289–296, 2002.

[28] V Körstgens, H-C Flemming, J Wingender, and W Borchard. Uniaxial compression measurement device for investigation of the mechanical stability of biofilms. *Journal of microbiological methods*, 46(1):9–17, 2001.

[29] Jan-Ulrich Kreft, Cristian Picioreanu, Julian WT Wimpenny, and Mark CM van Loosdrecht. Individual-based modelling of biofilms. *Microbiology*, 147(11):2897–2912, 2001.

[30] Young-Ju Lee and Jinchao Xu. New formulations, positivity preserving discretizations and stability analysis for non-newtonian flow models. *Computer methods in applied mechanics and engineering*, 195(9):1180–1206, 2006.

[31] Young-Ju Lee, Jinchao Xu, and Chen-Song Zhang. Stable finite element discretizations for viscoelastic flow models. *Handbook of numerical analysis*, 16:371–433, 2011.

[32] Alexei Lozinski and Robert G Owens. An energy estimate for the oldroyd b model: theory and applications. *Journal of Non-Newtonian Fluid Mechanics*, 112(2):161–176, 2003.

[33] Thien-Fah Mah, Betsey Pitts, Brett Pellock, Graham C Walker, Philip S Stewart, and George A O'Toole. A genetic basis for pseudomonas aeruginosa biofilm antibiotic resistance. *Nature*, 426(6964):306–310, 2003.

[34] Jerrold E Marsden and Thomas JR Hughes. *Mathematical foundations of elasticity*. Courier Corporation, 1994.

[35] Arturo A Massol-Deyá, Joanne Whallon, Robert F Hickey, and James M Tiedje. Channel structures in aerobic biofilms of fixed-film reactors treating contaminated groundwater. *Applied and Environmental Microbiology*, 61(2):769–777, 1995.

[36] Eberhard Morgenroth and Peter A Wilderer. Influence of detachment mechanisms on competition in biofilms. *Water Research*, 34(2):417–426, 2000.

[37] Nasim Muhammad and Hermann J Eberl. Openmp parallelization of a mickens time-integration scheme for a mixed-culture biofilm model and its performance on multi-core and multi-processor computers. In *High Performance Computing Systems and Applications*, pages 180–195. Springer, 2010.

[38] JG Oldroyd. On the formulation of rheological equations of state. 200(1063):523–541, 1950.

[39] Robert G Owens and Timothy N Phillips. *Computational rheology*, volume 14. World Scientific, 2002.

[40] Cristian Picioreanu, Jan-Ulrich Kreft, and Mark CM van Loosdrecht. Particle-based multidimensional multispecies biofilm model. *Applied and environmental microbiology*, 70(5):3024–3040, 2004.

[41] Cristian Picioreanu, M van Loosdrecht, and J Heijnen. *Multidimensional modeling of biofilm structure*. Delft University of Technology, Faculty of Applied Sciences, 1999.

[42] Cristian Picioreanu, Mark CM Van Loosdrecht, Joseph J Heijnen, et al. Mathematical modeling of biofilm structure with a hybrid differential-discrete cellular automaton approach. *Biotechnology and bioengineering*, 58(1):101–116, 1998.

[43] Cristian Picioreanu, Mark CM van Loosdrecht, Joseph J Heijnen, et al. A new combined differential-discrete cellular automaton approach for biofilm modeling: application for growth in gel beads. *Biotechnology and bioengineering*, 57(6):718–731, 1998.

[44] Cristian Picioreanu, JB Xavier, and Mark CM van Loosdrecht. Advances in mathematical modeling of biofilm structure. *Biofilms*, 1(04):337–349, 2004.

[45] Olivier Pironneau. On the transport-diffusion algorithm and its applications to the navier-stokes equations. *Numerische Mathematik*, 38(3):309–332, 1982.

[46] Prathish Rajaraman and Jeffrey J Heys. Simulation of nanoparticle transport in airways using petrov–galerkin finite element methods. *International journal for numerical methods in biomedical engineering*, 30(1):103–116, 2014.

[47] Junuthula Narasimha Reddy. *An introduction to the finite element method*, volume 2. McGraw-Hill New York, 1993.

[48] SS Rogers, C Van Der Walle, and TA Waigh. Microrheology of bacterial biofilms in vitro: Staphylococcus aureus and pseudomonas aeruginosa. *Langmuir*, 24(23):13549–13555, 2008.

[49] T Shaw, M Winston, CJ Rupp, I Klapper, and P Stoodley. Commonality of elastic relaxation times in biofilms. *Physical Review Letters*, 93(9):098102, 2004.

[50] Juan C Simo and Thomas JR Hughes. *Computational inelasticity*, volume 7. Springer Science & Business Media, 2006.

[51] Paul Stoodley, Zbigniew Lewandowski, John D Boyle, Hilary M Lappin-Scott, et al. Structural deformation of bacterial biofilms caused by short-term fluctuations in fluid shear: an in situ investigation of biofilm rheology. *Biotechnology and bioengineering*, 65(1):83–92, 1999.

[52] ENDRE SÜLI. A brief excursion into the mathematical theory of mixed finite element methods. *Lecture Notes, University of Oxford*, 2013.

[53] Cedric Taylor and P Hood. A numerical solution of the navier-stokes equations using the finite element technique. *Computers & Fluids*, 1(1):73–100, 1973.

[54] Brett W Towler, Cory J Rupp, AL B Cunningham, and Paul Stoodley. Viscoelastic properties of a mixed culture biofilm from rheometer creep analysis. *Biofouling*, 19(5):279–285, 2003.

[55] K Walters and MF Webster. The distinctive cfd challenges of computational rheology. *International journal for numerical methods in fluids*, 43(5):577–596, 2003.

[56] Zhi-Wu Wang and Shulin Chen. Potential of biofilm-based biofuel production. *Applied microbiology and biotechnology*, 83(1):1–18, 2009.

[57] Oskar Wanner, Hermann Eberl, Eberhard Morgenroth, Daniel Noguera, Cristian Picioreanu, Bruce Rittman, and Mark Loosdrecht. *Mathematical modeling of biofilms*, volume 18. IWA publishing, 2006.

[58] Oskar Wanner and Willi Gujer. A multispecies biofilm model. *Biotechnology and bioengineering*, 28(3):314–328, 1986.

[59] Frances Westall, Maarten J de Wit, Jesse Dann, Sjerry van der Gaast, Cornel EJ de Ronde, and Dane Gerneke. Early archean fossil bacteria and biofilms in hydrothermally-influenced sediments from the barberton greenstone belt, south africa. *Precambrian Research*, 106(1):93–116, 2001.

[60] Wikipedia. *Stokes Flow*, 2016 (accessed Oct 16, 2016).

[61] Wikipedia. *Viscoelasticity*, 2016 (accessed Oct 16, 2016).

[62] Kenneth Williamson and Perry L McCarty. A model of substrate utilization by bacterial films. *Journal (Water Pollution Control Federation)*, pages 9–24, 1976.